Electron Paramagnetic Resonance Spectroscopy

Electron paramagnetic resonance (EPR) spectroscopy was used to quantify vascular NO production according to previously described and validated methods.[30] In brief, freshly harvested aortas (n=8 to 11 per group) were stimulated with calcium ionophore (A23187; 1 μmol/L) in 100 μL Krebs–HEPES buffer, then incubated with colloid iron (II) diethyldithiocarbamate [$Fe(DETC)_2$] (285 μmol/L) at 37°C for 90 minutes. After incubation, aortas were snap-frozen in a column of Krebs–HEPES buffer in liquid nitrogen, and EPR spectra were obtained using an X-band EPR spectrometer (Miniscope MS 200; Magnettech). Signals were quantified by measuring the total amplitude, after correction of baseline, and after subtracting background signals from incubation with colloid $Fe(DETC)_2$ alone.

Lucigenin-Enhanced Chemiluminescence Detection of Superoxide in Heart Lysates

Basal $O_2^{\cdot-}$ production was measured in left ventricular (LV) homogenates (n=7 to 10 per group) using the technique of lucigenin (5 μmol/L) chemiluminescence according to methods described previously.[14,31] In brief, hearts were flushed with ice-cold Krebs–HEPES buffer, the LV excised, and snap-frozen in liquid nitrogen. Samples were homogenized in Kreb–HEPES buffer containing protease inhibitors (Complete; Boehringer Mannheim) at pH 7.4. Chemiluminescence was measured in a FB12 luminometer (Berthold Detection Systems) at 37°C. Chemiluminescence of 200 μg LV protein was recorded every minute for 8 minutes. The NOS inhibitor $N\omega$-nitro-L-arginine methyl ester hydrochloride (L-NAME; 1 mmol/L) was subsequently added and chemiluminescence recorded for an additional 5 minutes. Background readings were subtracted from sample readings and results expressed as counts per second.

Lucigenin-Enhanced Chemiluminescence Detection of Superoxide in Intact Aorta

Basal $O_2^{\cdot-}$ production was measured in intact aorta (n=8 to 12 per group) according to methods described previously.[14,32] In brief, freshly cleaned and harvested thoracic aortas were opened longitudinally, cut into 2, and transferred to ice-cold Krebs–HEPES buffer. Vessels were equilibrated in Krebs–HEPES buffer gassed with 95% oxygen/5% carbon dioxide for 30 minutes at 37°C, with one half of each vessel being incubated in the presence of L-NAME (1 mmol/L). Lucigenin (20 μmol/L) chemiluminescence was then recorded every minute for 10 minutes as above. Background readings were subtracted from sample readings and results expressed as counts per second per milligram dry weight of aorta.

Oxidative Fluorescent Microtopography

$O_2^{\cdot-}$ production in tissue sections of mouse aorta (n=5 to 7 per group) was detected using the fluorescent probe dihydroethidium (DHE), as described previously.[14,24,33] Fresh segments of thoracic aorta were frozen in optimal cutting temperature compound. Cryosections (30 μm) were incubated with Krebs–HEPES buffer with or without L-NAME (1 mmol/L; to inhibit eNOS) for 30 minutes at 37°C, then for an additional 5 minutes with DHE (2 μmol/L; Molecular Probes). Images were obtained using a Bio-Rad laser-scanning confocal microscope, equipped with a krypton/argon laser, using identical acquisition settings for each section. DHE fluorescence was quantified by automated image analysis using Image-Pro Plus software (Media Cybernetics). DHE fluorescence from high power (×60) images was measured only on the luminal side of the internal elastic lamina to quantify endothelial cell fluorescence. For each vessel, mean fluorescence was calculated from 4 separate high-power fields taken in each quadrant of the vessel to produce n=1, and all experiments were performed in a batch design.

Statistical Analysis

One-way ANOVA tests were used to compare data sets, with appropriate post hoc correction for multiple comparisons. $P<0.05$ was considered significant. Data are expressed as means and SEM.

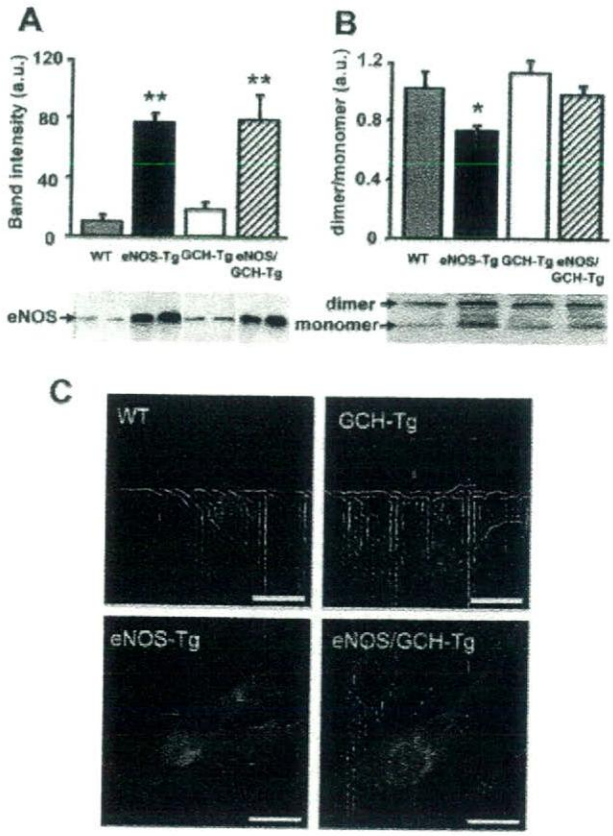

Figure 1. Immunoblotting with a murine anti-eNOS monoclonal antibody to detect native and transgenic eNOS monomer protein in boiled lung lysates (A) and eNOS dimer:monomer protein bands in aortic lysates from wild-type (WT), eNOS-Tg, GCH-Tg, and eNOS/GCH-Tg mice (B); n=4 animals per group; $^*P<0.05$ and $^{**}P<0.001$ compared with WT. a.u. indicates arbitrary units. C, Immunofluorescent detection of eNOS (green), counterstained with propidium iodide (red), in primary endothelial cells cultured from WT, eNOS-Tg, GCH-Tg, and eNOS/GCH-Tg mice. Bar=20 μm.

Results

eNOS Protein Levels and Subcellular Localization

Western blot analysis confirmed that eNOS protein levels were elevated 8-fold in eNOS-Tg compared with wild-type animals ($P<0.001$; Figure 1A). Overexpression of endothelial GTPCH, the rate-limiting enzyme in BH4 synthesis, in GCH-Tg mice did not significantly alter eNOS protein levels compared with wild type. However, as for eNOS-Tg mice, eNOS protein levels were elevated 8-fold in double-transgenic eNOS/GCH-Tg mice.

We used low-temperature SDS-PAGE and immunoblotting to investigate eNOS homodimerization and the ratio of eNOS dimer to monomer in aortas. In eNOS-Tg aortas, eNOS dimer:monomer was significantly depleted compared with wild type ($P<0.05$) but unchanged in GCH-Tg mice (Figure 1B). Importantly, the reduced eNOS dimer:monomer ratio in the eNOS-Tg group was restored to wild-type levels in double- transgenic eNOS/GCH-Tg mice.

We investigated the subcellular localization of eNOS in primary cultures of lung endothelial cells using immunocytochemistry. eNOS appeared to be localized mainly to plasma

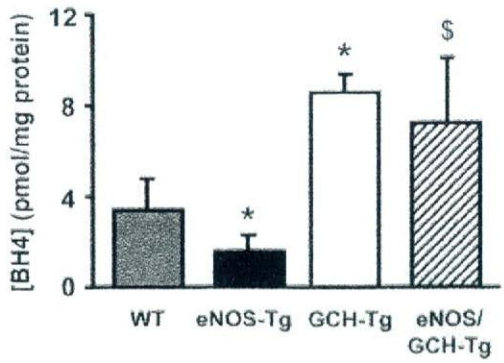

Figure 2. BH4 levels in aortas from wild-type (WT), eNOS-Tg, GCH-Tg, and eNOS/GCH-Tg mice. *$P<0.05$ compared with WT and \$$P<0.05$ compared with eNOS-Tg; n=6 to 8 animals per group.

membranes and the Golgi apparatus in endothelial cells from all 4 groups (Figure 1C). However, in accordance with the immunoblotting data, the intensity of eNOS immunostaining, unchanged in GCH-Tg mice, was markedly increased in endothelial cells from eNOS-Tg and eNOS/GCH-Tg animals compared with wild type.

Aortic BH4 Levels

We next measured vascular BH4 levels in homogenates of snap-frozen aorta using iodine oxidation and HPLC. Surprisingly, BH4 levels were significantly depleted in eNOS-Tg mice compared with wild type, suggesting oxidative degradation of BH4 ($P<0.05$; Figure 2). We then sought to confirm that increased endothelial GTPCH expression led to increased BH4 levels in aortic homogenates of GCH-Tg and eNOS/GCH-Tg mice. As reported previously,[24] aortic BH4 levels were significantly elevated by >2-fold in GCH-Tg mice compared with wild type ($P<0.05$). Importantly, aortic BH4 levels were also elevated in eNOS/GCH-Tg mice and were not significantly different between GCH-Tg and eNOS/GCH-Tg mice.

eNOS Enzymatic Activity and NO Production

To determine the relationship between eNOS protein levels and eNOS enzymatic activity, we measured conversion of ^{14}C L-arginine to ^{14}C L-citrulline by eNOS in intact aorta using HPLC with online scintillation detection. Citrulline production was increased only 2-fold in eNOS-Tg aortas compared with wild type ($P<0.05$; Figure 3A and 3B), despite eNOS protein levels being elevated 8-fold in these animals. Indeed, the ratio of eNOS enzymatic activity to eNOS protein was 0.6 in eNOS-Tg mice compared with 2.0 in wild-type animals. A similar pattern of results was obtained when using lung tissue lysates (Figure 3C). To further investigate the stoichiometric relationship between eNOS and endothelial BH4 in vivo and to determine whether increasing endothelial BH4 in eNOS-Tg mice could augment eNOS enzymatic activity, we next measured eNOS enzymatic activity in GCH-Tg and eNOS/GCH-Tg mice. NOS activity was increased 2-fold in GCH-Tg aorta and lung compared with wild type ($P<0.05$; Figure 3A through 3C). Indeed, eNOS enzymatic activity was similar in GCH-Tg and eNOS-Tg mice despite eNOS protein

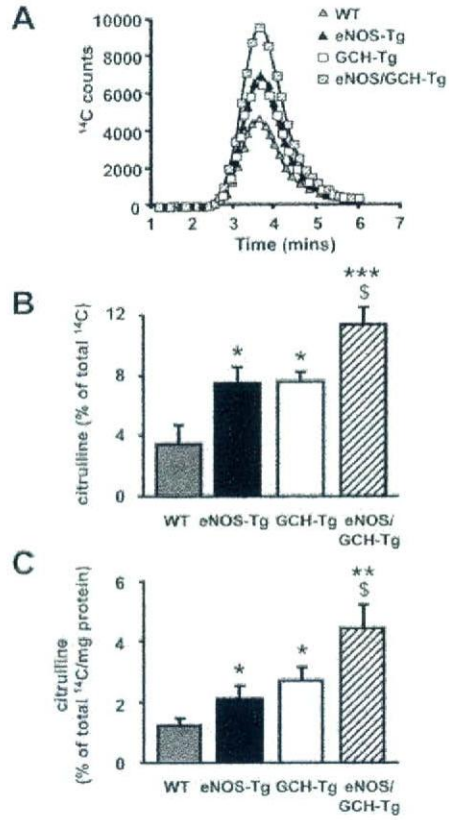

Figure 3. A, Representative HPLC chromatograms showing ^{14}C citrulline peaks for wild-type (WT; gray triangles), eNOS-Tg (black triangles), GCH-Tg (white squares), and eNOS/GCH-Tg (hatched squares) mouse aortas. Graphs show percentage ^{14}C citrulline conversion from ^{14}C arginine as a measure of eNOS activity measured in total fresh intact aorta (B) and lung tissue lysates (C); n=5 to 8 animals per group; *$P<0.05$, **$P<0.01$, and ***$P<0.001$ compared with WT; and \$$P<0.05$ compared with eNOS-Tg.

levels being considerably higher in eNOS-Tg animals. Critically, eNOS enzymatic activity was further elevated in eNOS/GCH-Tg mice compared with eNOS-Tg animals ($P<0.05$): augmented levels of endothelial BH4 in eNOS/GCH-Tg mice resulted in an ≈4-fold increase in eNOS enzymatic activity in aorta and lung compared with wild-type mice ($P<0.01$). These data suggest that eNOS activity is exquisitely dependent on endothelial BH4 levels even in the absence of vascular disease.

In complementary experiments, we used Fe-DETC EPR to directly measure NO bioavailability in mouse aortas. In accordance with measures of enzymatic activity, net NO levels were increased ≈2-fold in eNOS-Tg aortas compared with wild type (Figure 4). These results demonstrate that there was a striking discordance between eNOS protein levels, eNOS enzymatic activity, and NO production in eNOS-Tg mice. We then determined the effects of increased endothelial BH4 using the GCH-Tg and eNOS/GCH-Tg mice and observed a similar pattern of results as for NOS enzymatic activity. Aortic NO bioavailability was elevated almost 2-fold in GCH-Tg mice compared with wild type and not significantly different from eNOS-Tg mice (Figure 4). Criti-

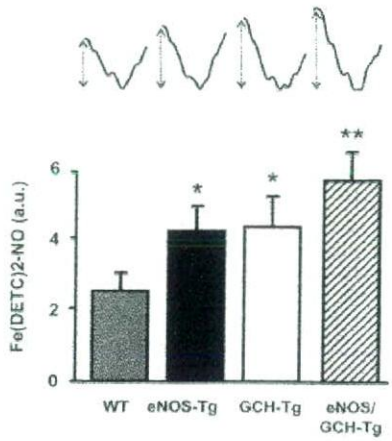

Figure 4. Net NO levels in intact aorta measured using Fe-DETC EPR. Graph shows mean quantitative data with corresponding representative EPR spectra showing the characteristic peaks associated with the Fe-DETC signal above. n=8 to 11 animals per group; *$P<0.05$ and **$P<0.01$ compared with wild type (WT). a.u. indicates arbitrary units.

cally, net NO bioavailability was further elevated (≈3-fold compared with wild type) in eNOS/GCH-Tg mice.

eNOS Uncoupling: Effect of eNOS and GTPCH Overexpression In Vivo

To investigate whether eNOS uncoupling results from discordance between eNOS and BH4, we measured $O_2^{\cdot-}$ production and, more specifically, eNOS-derived $O_2^{\cdot-}$ production using the NOS inhibitor L-NAME. We first measured $O_2^{\cdot-}$ production in tissue lysates using lucigenin chemiluminescence. Chemiluminescence was increased 2-fold in eNOS-Tg mice compared with wild-type animals ($P<0.05$; Figure 5A) but was unchanged in GCH-Tg mice. Critically, $O_2^{\cdot-}$ production was restored in eNOS/GCH-Tg mice. The proportion of $O_2^{\cdot-}$ production attributable to uncoupled NOS, assessed by quantifying L-NAME–inhibitable chemiluminescence, was significantly increased in eNOS-Tg lysates compared with wild type, indicating increased NOS uncoupling ($P<0.05$; Figure 5B). L-NAME–inhibitable chemiluminescence was unchanged in GCH-Tg mice. The presence of the GTPCH transgene in eNOS/GCH-Tg mice restored the enhanced L-NAME–inhibitable chemiluminescence of the eNOS-Tg group back to wild-type levels. We also investigated $O_2^{\cdot-}$ production in intact aorta under basal conditions and after incubation with L-NAME using lucigenin chemiluminescence and saw a similar pattern of results. Basal chemiluminescence was significantly increased in eNOS-Tg aortas compared with wild type ($P<0.05$; Table). Importantly, basal $O_2^{\cdot-}$ production in GCH-Tg and eNOS/GCH-Tg aortas was similar to wild type. Incubation of aortas with L-NAME caused a significant reduction in the $O_2^{\cdot-}$ signal in eNOS-Tg mice ($P<0.05$), indicating NOS uncoupling. However, L-NAME had little effect in wild-type, GCH-Tg, and eNOS/GCH-Tg aortas, suggesting that NOS coupling is preserved in these mice. Together, these observations suggest that in eNOS-Tg mice elevated $O_2^{\cdot-}$ production is at least partly attributable to uncoupled NOS, likely resulting from discordance between eNOS protein and endothelial BH4 because NOS coupling is preserved by increasing endothelial BH4 in association with elevated eNOS levels in eNOS/GCH-Tg animals.

Lucigenin Chemiluminescence to Measure $O_2^{\cdot-}$ Production in Intact Aortas Incubated for 30 Minutes at 37°C in the Presence or Absence of L-NAME (1 mmol/L)

	Wild Type	eNOS-Tg	GCH-Tg	eNOS/GCH-Tg
Basal, RLU/s/mg	39.5±4.5	59.7±6.6*	52.8±5.8	46.2±4.7
+ L-NAME, RLU/s/mg	42.5±10.1	39.2±4.8†	54.0±13.2	49.3±11.2

Results are expressed as counts per second per milligram of dry weight of aorta.

*$P<0.05$compared with wild type; †$P<0.05$ compared with baseline (without L-NAME).

RLU indicates relative light units.

To investigate $O_2^{\cdot-}$ production specifically from the aortic endothelium, we quantified endothelial DHE fluorescence using oxidative confocal microtopography. Endothelial DHE fluorescence was increased 2-fold in eNOS-Tg mice compared with wild-type and GCH-Tg mice (Figure 6). Impor-

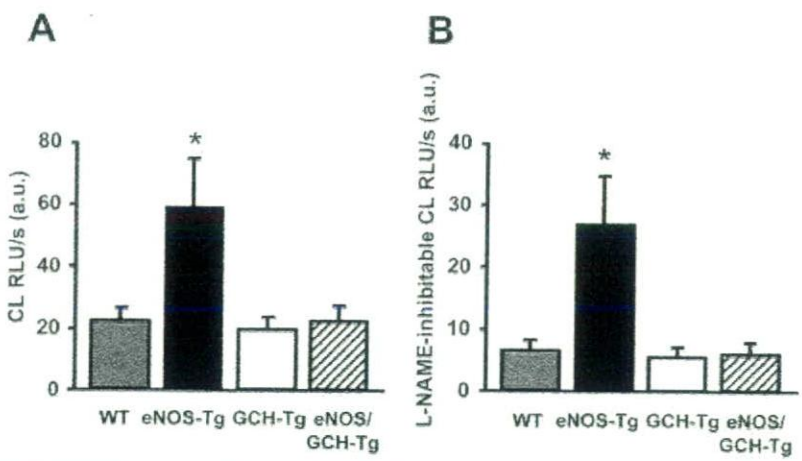

Figure 5. Lucigenin (5μmol/L) chemiluminescence (CL) in cardiac tissue lysates from wild-type (WT), eNOS-Tg, GCH-Tg, and eNOS/GCH-Tg mice to measure basal $O_2^{\cdot-}$ production (A) and L-NAME (1 mmol/L)–inhibitable $O_2^{\cdot-}$ production (B) as a marker of NOS uncoupling. *$P<0.05$ compared with WT; n=7 to 10 animals per group. RLU indicates relative light units; a.u., arbitrary units.

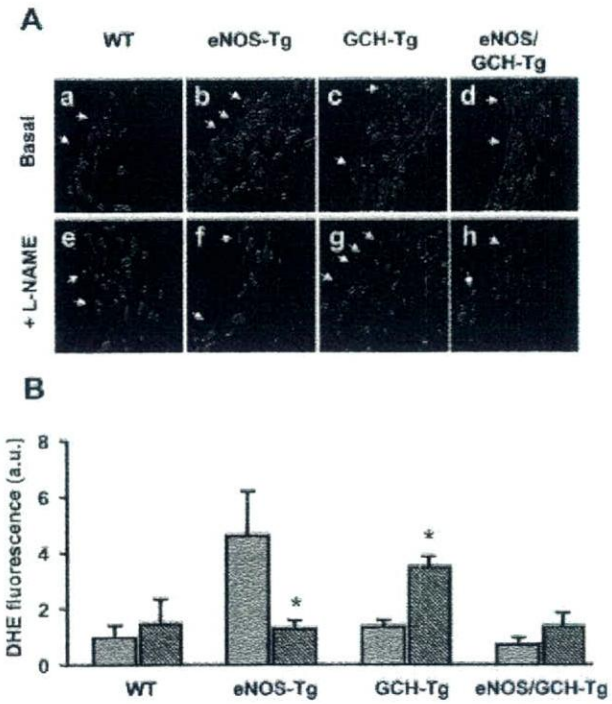

Figure 6. DHE staining, to measure in situ $O_2^{\cdot-}$ production, in aortic sections. A, Representative aortic sections (×60) showing red endothelial cells (arrows) from wild-type (WT; a and e), eNOS-Tg (b and f), GCH-Tg (c and g), and eNOS/GCH-Tg (d and h) mice in the presence (e through h) and absence (a through d) of L-NAME (1 mmol/L). B, Quantified specific endothelial DHE fluorescence is expressed for sections in the presence (hatched bars) and absence (gray bars) of L-NAME in arbitrary units (a.u.) for each group. *$P<0.05$ comparing sections in the presence or absence of L-NAME; n=5 to 7 animals per group.

tantly, endothelial fluorescence was restored to wild-type levels in eNOS/GCH-Tg mice. Fluorescence from the other layers of the vessel wall was not significantly different between groups. Incubation with L-NAME had little effect in wild-type aortas but reversed the elevated DHE signal in eNOS-Tg endothelium back to wild-type levels, again indicating that the source of $O_2^{\cdot-}$ was likely uncoupled eNOS. In contrast, L-NAME significantly increased the endothelial $O_2^{\cdot-}$ signal in GCH-Tg mice, indicating that in these aortas, eNOS was predominantly coupled and producing NO. Critically, as in wild-type aortas, NOS inhibition with L-NAME had little effect in eNOS/GCH-Tg mice, indicating restored eNOS coupling compared with eNOS-Tg animals. In accordance with the data for $O_2^{\cdot-}$ production measured by chemiluminescence, these results suggest that increased eNOS uncoupling in eNOS-Tg aortas increases eNOS-derived $O_2^{\cdot-}$, but that eNOS coupling is, at least in part, preserved by increased endothelial BH4 synthesis in eNOS/GCH-Tg mice.

Discussion

In this study, we describe a new double-transgenic mouse model in which endothelial-targeted overexpression of GTPCH leads to increased endothelial BH4 levels in mice with endothelial-targeted eNOS overexpression. We used this model to investigate the role of BH4 in the regulation of eNOS coupling in vivo, specifically in the absence of pathological oxidative stress associated with vascular disease states.[6] The major findings in this study are as follows. First, eNOS protein levels are markedly elevated in eNOS-Tg and eNOS/GCH-Tg mice but not in GCH-Tg animals, although the proportion of eNOS dimer to monomer is depleted only in eNOS-Tg aortas. Second, endothelial-specific overexpression of GTPCH is sufficient to increase vascular BH4 levels in GCH-Tg and in eNOS/GCH-Tg aortas, whereas BH4 levels are depleted in eNOS-Tg aortas. Third, this increase in BH4 is sufficient to augment vascular eNOS enzymatic activity even in GCH-Tg mice, which have unchanged eNOS protein levels. Indeed, eNOS activity is similar between GCH-Tg and eNOS-Tg mice despite eNOS-Tg mice having 8-fold more eNOS protein. Importantly, the increase in endothelial BH4 in eNOS/GCH-Tg mice further enhances eNOS activity and NO bioavailability compared with eNOS-Tg mice. Fourth, the discordance between endothelial BH4 and eNOS protein in eNOS-Tg mice results in uncoupled eNOS and increased NOS-derived $O_2^{\cdot-}$ production in tissue lysates and intact aorta. However, increased vascular BH4 in eNOS/GCH-Tg mice is sufficient, at least in part, to restore eNOS coupling, increase NO production, and reduce eNOS-dependent $O_2^{\cdot-}$ production.

These findings provide important insights into the role of endothelial BH4 synthesis in regulating eNOS activity and eNOS coupling even in the absence of vascular oxidative stress. Previous studies have reported that endothelial dysfunction in vascular diseases, such as hypertension,[12] diabetes,[24] and atherosclerosis,[26] is associated with increased $O_2^{\cdot-}$ production deriving principally from NADPH oxidases.[7,8] Landmesser et al[12] demonstrated that the increase in NADPH oxidase–derived $O_2^{\cdot-}$ in deoxycorticosterone acetate–salt hypertensive mice led to enhanced oxidation of BH4, resulting in eNOS uncoupling, increased eNOS-derived $O_2^{\cdot-}$ production, and reduced NO formation, thereby exacerbating oxidative stress. Oral supplementation with BH4, or a reduction in NADPH oxidase activity (using p47phox−/− mice), reversed eNOS uncoupling. However, the mechanistic relationship between eNOS and its cofactor BH4 has not been investigated in vivo in the absence of pathological oxidative stress. We now show that a stoichiometric discordance between eNOS protein and BH4 levels is alone sufficient to cause eNOS uncoupling, and that eNOS uncoupling in the absence of vascular disease is sufficient to deplete BH4 levels by oxidation. Laursen et al[19] demonstrated that peroxynitrite may be the principal ROS involved in oxidation of BH4.

NO, constitutively produced by eNOS in the vascular endothelium, is a potent vasodilator and exerts numerous vasoprotective antiatherogenic effects. Reduced NO bioactivity is an early feature of a number of vascular diseases, including atherosclerosis.[5] Short-term in vivo gene transfer of eNOS or neuronal NOS can improve NO-mediated vascular relaxation in atherosclerotic arteries.[34] However, previous studies investigating the possible vasoprotective effects of chronic eNOS overexpression in eNOS-Tg mice have yielded conflicting results. Kawashima et al[35] demonstrated reduced lesion formation after carotid artery ligation in eNOS-Tg mice. In contrast, Ozaki et al,[10] using the same strain of

eNOS-Tg mice as used in the present study, found that eNOS overexpression accelerated rather than reduced atherosclerosis in apolipoprotein E knockout mice, at least in part, because of eNOS uncoupling and $O_2^{\cdot-}$ generation. In the present study, using a mouse model not exposed to pathological vascular oxidative stress, we also show that eNOS-derived $O_2^{\cdot-}$ production is enhanced in eNOS-Tg mice, in cardiac tissue lysates and intact aorta, indicating increased eNOS uncoupling in these animals. We performed additional experiments, using quantitative RT-PCR, to confirm that the increased $O_2^{\cdot-}$ in eNOS-Tg animals is not a result of a concomitant increase in the expression of the NADPH oxidase system, a major source of vascular $O_2^{\cdot-}$ generation (data not shown). These findings agree with those from Ohashi et al[25] using nondiseased eNOS-Tg mice. This enhanced vascular oxidative stress may account for the depleted aortic BH4 levels observed in the eNOS-Tg mice because BH4 is readily oxidized by ROS to BH2 that is inactive for eNOS cofactor function. In accordance with having increased uncoupled eNOS and depleted BH4 levels, specific NOS enzymatic activity is markedly attenuated in eNOS-Tg mice (elevated only 2-fold compared with wild type) relative to eNOS protein levels (elevated 8-fold compared with wild type). Indeed, the ratio of eNOS enzymatic activity to eNOS protein was only 0.6 in eNOS-Tg mice compared with 2.0 in wild-type animals.

Several previous studies have established that BH4 is a required cofactor for NOS activity.[9,28,36] Recent studies, including those in atherosclerotic eNOS-Tg mice,[10] have demonstrated that NOS uncoupling can be reversed and NOS enzymatic activity increased by augmenting BH4 levels.[10,12] However, an advantage of the present study is that by targeting overexpression of GTPCH, the rate-limiting enzyme in BH4 biosynthesis, to the vascular endothelium, we avoid the potential confounding antioxidant effects of high-dose pharmacological BH4 supplementation used in other studies.[10,12] Furthermore, we have been able to specifically evaluate the role of endothelial BH4, as opposed to systemic BH4, in the regulation of eNOS activity. Importantly, using 2 methods to measure $O_2^{\cdot-}$ production in cardiac tissue and intact aorta, as well as specifically in aortic endothelium, we demonstrate that NOS-dependent $O_2^{\cdot-}$ generation, elevated in eNOS-Tg mice, is normalized in eNOS/GCH-Tg mice. These data support the hypothesis that discordance between eNOS protein and endothelial BH4 levels is sufficient to cause eNOS uncoupling even in the absence of pathological oxidative stress. In support of this conclusion, NOS enzymatic activity and the ratio of enzymatic activity relative to eNOS protein levels were increased in eNOS/GCH-Tg compared with eNOS-Tg mice. Interestingly, GCH-Tg mice also had increased NOS enzymatic activity compared with wild type, indicating that even in the absence of either enhanced eNOS protein or disease, BH4 levels may limit eNOS enzymatic activity in vivo. These data therefore suggest that eNOS activity (to generate NO) can be augmented by modestly increasing BH4 levels, specifically in the endothelium, even under normal physiological conditions.

Previous data have shown that eNOS dimerization is an important aspect of eNOS activation and NO production.[28] BH4 has been suggested to increase the stability of the eNOS homodimer such that the ratio of dimer to monomer is increased.[28,37] In eNOS-Tg mice, the discordance between high levels of eNOS protein and depleted aortic BH4 levels may account for the relative decrease in homodimeric eNOS protein that we observed. In support, the increased production of endothelial BH4 in eNOS/GCH-Tg mice was sufficient to maintain the ratio of eNOS dimer to monomer. These in vivo findings corroborate previous in vitro studies suggesting that an important action of BH4, in addition to its direct contribution to electron transport within the eNOS active site, is to maintain eNOS in its homodimeric conformation.

We conclude that eNOS uncoupling is an independent and direct consequence of a stoichiometric discordance between enzyme and its cofactor BH4. BH4 is critical for regulating eNOS activity and its production of NO, as opposed to $O_2^{\cdot-}$, even in the absence of increased oxidative stress associated with vascular disease states. Thus, strategies to increase eNOS protein without a concomitant augmentation of endothelial BH4 levels may lead to eNOS uncoupling and paradoxically exacerbate oxidative stress and the progression of vascular diseases. Although reduced biosynthesis of BH4 may not be the principal mechanism of BH4 loss in vascular disease, strategies aimed at increasing BH4 synthesis or reducing BH4 oxidation may be valid therapeutic approaches in vascular disease states.

Acknowledgments

This work was supported by the British Heart Foundation (RG02/007) and the Wellcome Trust.

References

1. Ignarro LJ. Nitric oxide as a unique signaling molecule in the vascular system: a historical overview. *J Physiol Pharmacol*. 2002;53:503–514.
2. Furchgott RF, Zawadzki JV. The obligatory role of endothelial cells in the relaxation of arterial smooth muscle by acetylcholine. *Nature*. 1980;288:373–376.
3. Panza JA, García CE, Kilcoyne CM, Quyyumi AA, Cannon RO III. Impaired endothelium-dependent vasodilation in patients with essential hypertension: evidence that nitric oxide abnormality is not localized to a single signal transduction pathway. *Circulation*. 1995;91:1732–1738.
4. Schachinger V, Britten MB, Zeiher AM. Prognostic impact of coronary vasodilator dysfunction on adverse long-term outcome of coronary heart disease. *Circulation*. 2000;101:1899–1906.
5. Heitzer T, Schlinzig T, Krohn K, Meinertz T, Munzel T. Endothelial dysfunction, oxidative stress, and risk of cardiovascular events in patients with coronary artery disease. *Circulation*. 2001;104:2673–2678.
6. Cai H, Harrison DG. Endothelial dysfunction in cardiovascular diseases: the role of oxidant stress. *Circ Res*. 2000;87:840–844.
7. Griendling KK, Sorescu D, Ushio-Fukai M. NAD(P)H oxidase: role in cardiovascular biology and disease. *Circ Res*. 2000;86:494–501.
8. Guzik TJ, West NEJ, Black E, McDonald D, Ratnatunga C, Pillai R, Channon KM. Vascular superoxide production by NAD(P)H oxidase: association with endothelial dysfunction and clinical risk factors. *Circ Res*. 2000;86:e85–e90.
9. Vasquez-Vivar J, Kalyanaraman B, Martasek P, Hogg N, Masters BS, Karoui H, Tordo P, Pritchard KA Jr. Superoxide generation by endothelial nitric oxide synthase: the influence of cofactors. *Proc Natl Acad Sci U S A*. 1998;95:9220–9225.
10. Ozaki M, Kawashima S, Yamashita T, Hirase T, Namiki M, Inoue N, Hirata K-i, Yasui H, Sakurai H, Yoshida Y, Masada M, Yokoyama M. Overexpression of endothelial nitric oxide synthase accelerates atherosclerotic lesion formation in apoE-deficient mice. *J Clin Invest*. 2002;110:331–340.
11. Vasquez-Vivar J, Kalyanaraman B, Martasek P. The role of tetrahydrobiopterin in superoxide generation from eNOS: enzymology and physiological implications. *Free Radic Res*. 2003;37:121–127.

12. Landmesser U, Dikalov S, Price SR, McCann L, Fukai T, Holland SM, Mitch WE, Harrison DG. Oxidation of tetrahydrobiopterin leads to uncoupling of endothelial cell nitric oxide synthase in hypertension. *J Clin Invest*. 2003;111:1201–1209.
13. Maier W, Cosentino F, Lutolf RB, Fleisch M, Seiler C, Hess OM, Meier B, Luscher TF. Tetrahydrobiopterin improves endothelial function in patients with coronary artery disease. *J Cardiovasc Pharmacol*. 2000;35:173–178.
14. Guzik TJ, Mussa S, Gastaldi D, Sadowski J, Ratnatunga C, Pillai R, Channon KM. Mechanisms of increased vascular superoxide production in human diabetes mellitus: role of NAD(P)H oxidase and endothelial nitric oxide synthase. *Circulation*. 2002;105:1656–1662.
15. Heitzer T, Yla-Herttuala S, Luoma J, Kurz S, Munzel T, Just H, Olschewski M, Drexler H. Cigarette smoking potentiates endothelial dysfunction of forearm resistance vessels in patients with hypercholesterolemia. Role of oxidized LDL. *Circulation*. 1996;93:1346–1353.
16. Alp NJ, Channon KM. Regulation of endothelial nitric oxide synthase by tetrahydrobiopterin in vascular disease. *Arterioscler Thromb Vasc Biol*. 2004;24:413–420.
17. Vasquez-Vivar J, Whitsett J, Martasek P, Hogg N, Kalyanaraman B. Reaction of tetrahydrobiopterin with superoxide: EPR-kinetic analysis and characterization of the pteridine radical. *Free Radic Biol Med*. 2001;31:975–985.
18. Zheng J-S, Yang X-Q, Lookingland KJ, Fink GD, Hesslinger C, Kapatos G, Kovesdi I, Chen AF. Gene transfer of human guanosine 5′-triphosphate cyclohydrolase I restores vascular tetrahydrobiopterin level and endothelial function in low renin hypertension. *Circulation*. 2003;108:1238–1245.
19. Laursen JB, Somers M, Kurz S, McCann L, Warnholtz A, Freeman BA, Tarpey M, Fukai T, Harrison DG. Endothelial regulation of vasomotion in apoE-deficient mice: implications for interactions between peroxynitrite and tetrahydrobiopterin. *Circulation*. 2001;103:1282–1288.
20. Kuzkaya N, Weissmann N, Harrison DG, Dikalov S. Interactions of peroxynitrite, tetrahydrobiopterin, ascorbic acid, and thiols: implications for uncoupling endothelial nitric-oxide synthase. *J Biol Chem*. 2003;278:22546–22554.
21. Vasquez-Vivar J, Martasek P, Whitsett J, Joseph J, Kalyanaraman B. The ratio between tetrahydrobiopterin and oxidized tetrahydrobiopterin analogues controls superoxide release from endothelial nitric oxide synthase: an EPR spin trapping study. *Biochem J*. 2002;362:733–739.
22. Vasquez-Vivar J, Martasek P, Kalyanaraman B. Superoxide generation from nitric oxide synthase: role of cofactors and protein interaction. In: *Biological Magnetic Resonance*. Boston, Mass: Kluwer Academic Publishers; 2005:75–91.
23. Rodriguez-Crespo I, Gerber NC, Ortiz de Montellano PR. Endothelial nitric-oxide synthase. Expression in *Escherichia coli*, spectroscopic characterization, and role of tetrahydrobiopterin in dimer formation. *J Biol Chem*. 1996;271:11462–11467.
24. Alp NJ, Mussa S, Khoo J, Guzik TJ, Cai S, Jefferson A, Rockett KA, Channon KM. Tetrahydrobiopterin-dependent preservation of nitric oxide-mediated endothelial function in diabetes by targeted transgenic GTP-cyclohydrolase I overexpression. *J Clin Invest*. 2003;112:725–735.
25. Ohashi Y, Kawashima S, Hirata K, Yamashita T, Ishida T, Inoue N, Sakoda T, Kurihara H, Yazaki Y, Yokoyama M. Hypotension and reduced nitric oxide-elicited vasorelaxation in transgenic mice overexpressing endothelial nitric oxide synthase. *J Clin Invest*. 1998;102:2061–2071.
26. Alp NJ, McAteer MA, Khoo J, Choudhury RP, Channon KM. Increased endothelial tetrahydrobiopterin synthesis by targeted transgenic GTP-cyclohydrolase I overexpression reduces endothelial dysfunction and atherosclerosis in ApoE-knockout mice. *Arterioscler Thromb Vasc Biol*. 2004;24:445–450.
27. Klatt P, Schmidt K, Lehner D, Glatter O, Bachinger HP, Mayer B. Structural analysis of porcine brain nitric oxide synthase reveals a role for tetrahydrobiopterin and L-arginine in the formation of an SDS- resistant dimer. *EMBO J*. 1995;14:3687–3695.
28. Cai S, Alp NJ, Mc Donald D, Canevari L, Heales S, Channon KM. GTP cyclohydrolase I gene transfer augments intracellular tetrahydrobiopterin in human endothelial cells: effects on nitric oxide synthase activity, protein levels and dimerization. *Cardiovasc Res*. 2002;55:838–849.
29. Rockett KA, Brookes R, Udalova I, Vidal V, Hill AV, Kwiatkowski D. 1,25-Dihydroxyvitamin D3 induces nitric oxide synthase and suppresses growth of Mycobacterium tuberculosis in a human macrophage-like cell line. *Infect Immun*. 1998;66:5314–5321.
30. Kleschyov AL, Munzel T. Advanced spin trapping of vascular nitric oxide using colloid iron diethyldithiocarbamate. *Methods Enzymol*. 2002;359:42–51.
31. Bendall JK, Heymes C, Wright TJ, Wheatcroft S, Grieve DJ, Shah AM, Cave AC. Strain-dependent variation in vascular responses to nitric oxide in the isolated murine heart. *J Mol Cell Cardiol*. 2002;34:1325–1333.
32. Skatchkov MP, Sperling D, Hink U, Mulsch A, Harrison DG, Sindermann I, Meinertz T, Munzel T. Validation of lucigenin as a chemiluminescent probe to monitor vascular superoxide as well as basal vascular nitric oxide production. *Biochem Biophys Res Commun*. 1999;254:319–324.
33. Khan SA, Lee K, Minhas KM, Gonzalez DR, Raju SVY, Tejani AD, Li D, Berkowitz DE, Hare JM. Neuronal nitric oxide synthase negatively regulates xanthine oxidoreductase inhibition of cardiac excitation-contraction coupling. *Proc Natl Acad Sci U S A*. 2004;101:15944–15948.
34. Channon KM, Qian HS, Neplioueva V, Blazing MA, Olmez E, Shetty GA, Youngblood SA, Stamler JS, George SE. In vivo gene transfer of nitric oxide synthase enhances vasomotor function in carotid arteries from normal and cholesterol-fed rabbits. *Circulation*. 1998;98:1905–1911.
35. Kawashima S, Yamashita T, Ozaki M, Ohashi Y, Azumi H, Inoue N, Hirata K-i, Hayashi Y, Itoh H, Yokoyama M. Endothelial NO synthase overexpression inhibits lesion formation in mouse model of vascular remodeling. *Arterioscler Thromb Vasc Biol*. 2001;21:201–207.
36. Tzeng E, Billiar TR, Robbins PD, Loftus M, Stuehr DJ. Expression of human inducible nitric oxide synthase in a tetrahydrobiopterin (H4B)-deficient cell line—H4B promotes assembly of enzyme subunits into an active enzyme. *Proc Natl Acad Sci U S A*. 1995;92:11771–11775.
37. Wever RMF, van Dam T, van Rijn HJ, de Groot F, Rabelink TJ. Tetrahydrobiopterin regulates superoxide and nitric oxide generation by recombinant endothelial nitric oxide synthase. *Biochem Biophys Res Commun*. 1997;237:340–344.

ELSEVIER

Cardiovascular Research 68 (2005) 249 – 258

Cardiovascular Research

www.elsevier.com/locate/cardiores

Xenogenic smooth muscle cell immunization reduces neointimal formation in balloon-injured rabbit carotid arteries

Masakazu Shinohara, Seinosuke Kawashima *, Tomoya Yamashita, Tomofumi Takaya, Ryuji Toh, Tatsuro Ishida, Tomomi Ueyama, Nobutaka Inoue, Ken-ichi Hirata, Mitsuhiro Yokoyama

Division of Cardiovascular and Respiratory Medicine, Department of Internal Medicine, Kobe University Graduate School of Medicine, 7-5-1 Kusunoki-cho, Chuo-ku, Kobe 650-0017, Japan

Received 6 October 2004; received in revised form 20 June 2005; accepted 22 June 2005
Available online 21 July 2005
Time for primary review 20 days

Abstract

Objective: Intimal hyperplasia plays an important role in a variety of types of vascular remodeling, particularly luminal narrowing after vascular injury. The vascular smooth muscle cells (VSMCs) in the neointimal area are a synthetic phenotype and have different epitopes from VSMCs in the normal media. The synthetic VSMCs in the neointima contain various possible antigens that can be targeted by the immune system. In this study, we tried to develop a new immunotherapy, which targets the synthetic VSMCs, for prevention of neointimal formation after angioplasty.

Method and results: Rabbits were repeatedly immunized with fixed xenogenic rat cultured VSMCs suspended in adjuvant as immunogens or injected with adjuvant and phosphate-buffered saline (PBS) or rat hepatocytes as controls every 2 weeks for 3 times. One week after the last immunization/injection, balloon injury of the left common carotid artery was performed. Four weeks after the injury, rabbits were euthanized and the neointimal lesion formation was assessed. The mean neointimal area of the PBS-injected, non-immunized group and the rat hepatocyte-immunized, control group was not statistically different (0.339 ± 0.036 and 0.350 ± 0.041 mm^2, P=NS). However, immunization with rat VSMCs significantly reduced the intimal lesion area (0.219 ± 0.0286 mm^2; $P < 0.05$ vs. PBS-injected, non-immunized group and rat hepatocyte-immunized group.) PCNA-immunopositive proliferating VSMCs in the neointima were suppressed by the rat VSMC immunization ($1.34 \pm 0.49\%$ vs. $5.78 \pm 0.47\%$; $P < 0.05$ vs. PBS-injected, non-immunized group). Rat VSMC immunization induced antibodies which had strong cross-reactivity against rabbit synthetic VSMCs. In experiments in vitro, proliferation and migration of rabbit VSMCs that were stimulated by serum, angiotensin (AT) II, platelet-derived growth factor (PDGF)-BB, fibroblast growth factor (FGF), and the phorbol ester PMA were significantly suppressed by treatment with immunoglobulin extracted from the VSMC-immunized rabbit plasma, implying that the immunoglobulin had some global effects on VSMCs. The rat VSMC-immunized rabbit immunoglobulin bound the rabbit AT1a receptor protein, which was expressed in COS7 cells by transfection of rabbit AT1a receptor pcDNA3. This binding to AT1a receptor may be one of mechanisms of the effects of VSMC-immunized immunoglobulin.

Conclusion: Xenogenic, synthetic rat VSMC immunization in rabbits induced auto-antibodies against synthetic rabbit VSMCs in a cross-reaction. The induced auto-antibodies against synthetic VSMCs may provide a possibility of new immunotherapy for vascular remodeling that forms neointimal lesions.

Keywords: Neointimal formation; Vascular remodeling; Vascular smooth muscle; Antibody; Immunotherpy

* Corresponding author. Tel.: +81 78 382 5846; fax: +81 78 382 5859.
E-mail address: kawashim@med.kobe-u.ac.jp (S. Kawashima).

0008-6363/$ - see front matter © 2005 European Society of Cardiology. Published by Elsevier B.V. All rights reserved.
doi:10.1016/j.cardiores.2005.06.016

This article is referred to in the Editorial by Thaunat et al. (pages 183–185) in this issue.

1. Introduction

Intimal hyperplasia plays an important role in a variety of types of vascular remodeling, particularly luminal narrowing after vascular injury such as that seen in restenosis following percutaneous coronary intervention. Proliferation and migration of vascular smooth muscle cells (VSMCs) from the media play a central role in neointimal formation, and various strategies have been developed to inhibit it, including inhibition of cell cycle of VSMCs, induction of apoptosis of VSMCs, and inhibition of intracellular signal transduction in VSMCs [1–4].

Recently immunological modulation has attracted attention as a possible therapeutic strategy of atherosclerosis [5–22]. Although only limited information is available, several studies have shown the possibility of immunotherapy against neointimal lesion formation after balloon injury. It seems that adequate induction of B-lymphocyte-related immunity has potential beneficial effects on neointimal formation. Nilsson et al. showed that immunization with homologous oxidized low density lipoprotein reduced neointimal formation after balloon injury in hypercholesterolemic rabbits [23]. In balloon-injured rat carotid arteries, it was demonstrated that treatment with an anti-P selectin monoclonal antibody reduced inflammation, in neointimal formation, and vascular remodeling [24]. However, until now, only few epitopes have been reported as appropriate targets of immunotherapy against neointimal formation.

It is possible that synthetic VSMCs in the neointima contain various possible antigens that can be targeted by the immune system. Since VSMCs play a central role in neointimal formation, we hypothesized that immune modulation targeting the synthetic VSMCs-associated antigens may inhibit neointimal formation after balloon injury. To prove this hypothesis, rabbits were immunized with the synthetic xenogenic rat VSMCs and then balloon-injured to induce neointimal formation.

2. Methods

2.1. Materials and animals

All drugs and culture media used in this study were purchased from Sigma Chemical Co. (MO) and WAKO (Japan). Male Japanese White Rabbits were purchased from a breeder (SLC, Hamamatsu, Japan) and kept under conventional conditions in our animal facility. Rabbits were fed normal chow (Oriental Yeast, Japan) and water ad libitum and maintained on a 12 h light/dark cycle. All animal experiments were conducted according to the "Guidelines for Animal Experiments at Kobe University Graduate School of Medicine", which complies NIH Guidelines.

2.2. Preparation for rat vascular smooth muscle cells and rat hepatocytes as immunogens

Rat VSMCs were prepared from thoracic aortas of male Sprague–Dawley rats by the collagenase digestion method and cultured as described [25]. For all experiments, rat aortic VSMCs from passage 5 to 8 were used. Rat hepatocytes (RLC-18, Cell No. RCB1484) were purchased from Rikken Cell Bank (Japan).

Rat VSMCs and rat hepatocytes were cultured in DMEM with 10% fetal bovine serum (FBS), and approximately 1×10^8 cells were collected and washed three times with phosphate buffered saline (PBS). The cells were fixed with 10% neutralized formaldehyde (WAKO, Japan) for 24 h at 4 °C. After being washed three times and incubated at 37 °C for 2 h to remove residual formaldehyde, the cells were washed again and re-suspended in PBS for use as immunogens.

2.3. Experimental protocol

Male Japanese White Rabbits (body weights were 2.0 kg) were divided into three groups. Injection of either rat VSMCs as immunogens (1×10^8 cells per rabbit), vehicle PBS for control non-immunized group or rat hepatocytes (1×10^8 cells per rabbit) for control immunized group was started. Those injections were subcutaneously performed in the rabbits' back with an equal volume of adjuvant every two weeks for three times. We used the Freund complete adjuvant for the first immunization, and the Freund incomplete adjuvant for the second and the third immunization.

One week after the last injection, rabbits were anesthetized with sodium pentothal. Blood sample was collected from the ear vein. Plasma immunoglobulin (IgG) levels were assessed using a commercially available kit (Bethyl Laboratories Inc. TX). A 2F Fogarty embolectomy catheter (Baxter, USA) was introduced through an aseptic neck incision produced in the facial branch of the external left carotid artery and positioned approximately at the origin of the common carotid artery. An acute balloon injury was performed by inflating the balloon with 0.1 mL saline solution and then gently pulling it back along the entire length of the common carotid artery with constant rotation as described before [26]. The catheter was then removed, the artery branch was ligated, and the surgical wound was closed. Two and four weeks after balloon injury, rabbits were euthanized, and the neointimal lesion formation was assessed.

2.4. Histological and immunohistochemical analysis of neointimal lesions

Serial equally spaced cross sections (5 μm thick) were obtained throughout the entire length of the carotid artery

for histological analysis (average of six sections per animal). All samples were routinely stained with hematoxyline and eosin or subjected to immunostaining with the anti-proliferating cell nuclear antigen (PCNA). For immunohistochemistry, slides were preincubated with 1% bovine serum to decrease nonspecific binding. Sections were incubated overnight at 4 °C with the mouse anti-PCNA antibody (DAKO, Denmark).

2.5. Quantification of neointimal lesions in sections of carotid arteries

Six equally spaced cross sections of the entire length of carotid arteries were used in all rabbits to quantify neointimal lesions. Using NIH imaging software, total cross-sectional neointimal area was measured between the endothelial cell monolayer and the internal elastic lamina. Total cross-sectional medial area was measured between the external and internal elastic lamina.

2.6. Quantification of proliferating neointimal cells

Serial cross sections (5 μm thickness) of carotid arteries were made. One section was used for HE-staining to calculate the total cell number in the neointimal area, and the next section was used for PCNA immunohistochemistry. The total PCNA-immunopositive neointimal cells and total neointimal cells in HE-staining in each serial section were counted. Then, the percentage of PCNA-immunopositive cells per total number of neointimal cells in each section was calculated, and the average of the six sections per animal was obtained for each animal.

2.7. Detection of apoptosis in the neointimal cells

Apoptosis in the neointimal cells was detected by TUNEL technique. Modified TUNEL assay was performed by use of DeadEnd colorimetric apoptosis detection system (Promega) according to the manufacturer's instructions. Briefly, tissue sections from the neointima of PBS injected non-immunized group and rat VSMC-immunized group were washed in PBS, and endogenous peroxidase was blocked by 0.3% hydrogen peroxide. Biotinylated nucleotide was incorporated at the 3′-OH DNA ends using terminal deoxynucleotidyl transferase (TdT). Streptavidin-HRP was then bound to these biotinylated nucleotides, which were detected using hydrogen peroxide and diaminobenzidine (DAB). Some of slides were treated with Dnase I for positive controls. Stained cells were counted under a light microscope.

2.8. Immunoglobulin purification from rabbit plasma

The immunoglobulin from the pooled plasma derived from the rabbits on day 7 after the third immunization or from control rabbits was purified with the use of a Protein G column (Sigma, MO).

2.9. Immunoblotting using rabbit plasma and protein analysis

Rabbit VSMCs were primarily cultured by the explant method and cultured in DMEM with 10% fetal bovine serum (FBS). Rabbit VSMCs were homogenized in a homogenizing buffer containing 50 mM Tris–HCl (pH 7.4), 1 mM EDTA, 1 mM phenylmethyosulfonylfluoride, 10% glycerol, and 20 mM CHAPS. The whole protein (50 μg per lane) was resolved by SDS-PAGE (10% polyacrylamide), transferred to a PVDF membrane and probed with rabbit plasma obtained from PBS injected non-immunized control rabbits, rat hepatocyte-immunized control rabbits, or rat VSMC-immunized rabbits. Immunoreactive bands were visualized with horseradish peroxidase-conjugated anti-rabbit IgG (Amersham, England; 1:3000 dilution) and an ECL detection kit (Amersham, England).

2.10. Counting of VSMC number in vitro

Cell proliferation was quantified by total cell number as previously described [27]. Rabbit VSMCs (5000 per well) were seeded in 96-well microtiter plates in 0.1 mL of DMEM–10% FBS. After 12 h incubation, the medium was replaced by DMEM with purified immunoglobulin from rat hepatocyte-immunized group and that from rat VSMC-immunized group (20 μg/mL, respectively). At 48 h after stimulation with agonists (10% FBS, 1 μM ATII, 10 ng/ml PDGF-BB, 10 ng/ml FGF, 1 μM PMA), cells were fixed by addition of 10 μL of glutaraldehyde and shaken for 15 min. After being washed 3 times with deionized water, plates were air-dried and stained for 20 min with 0.1% crystal violet solution in 200 mM MES, pH 6.0. After being washed 3 times with deionized water to remove excess dye, plates were air-dried before solubilization of the bound dye in 10% acetic acid. The optical density of dye extracts was measured at 595 nm by using a microplate reader (Bio-Rad). Values are means ± SEM of 8 separate experiments in each group.

2.11. VSMC migration

Rabbit VSMCs were grown to confluence in 6-well culture plates. The monolayer-wounding cell migration assay was performed as described previously [28,29]. Cell layers were scraped with a sterile single edged razor blade and re-incubated in DMEM containing 5 mM hydroxyurea with purified immunoglobulin from rat hepatocyte-immunized rabbits or rat VSMC-immunized rabbits (20 μg/mL, respectively). Hydroxyurea was added to eliminate any confounding effects of cell proliferation. At 24 h after stimulation with agonists (10% FBS, 1 μM ATII, 10 ng/ml PDGF-BB, 10 ng/ml FGF, 1 μM PMA), cells were fixed and the maximum migration distance across the wound edge was analyzed.

2.12. VSMC viability assay

Rabbit VSMCs (5000 per well) were incubated in 96-well plastic plates with purified immunoglobulin from rat VSMC-immunized rabbits or rat hepatocyte-immunized rabbits (20 μg/mL, respectively). After 24 h, cell viability was assessed by measuring mitochondrial NADH-dependent dehydrogenase activity with a Cell Counting Kit (Dojindo Molecular Technologies, Inc., Kumamoto, Japan) using sulfonated tetrazolium salt, 2-(4-iodophenyl)-3-(4-nitrophenyl)-5-(2,4-disulfophenyl)-2H-tetrazolium monosodium salt (WST-1) [30]. Each measurement was done in triplicate and the results

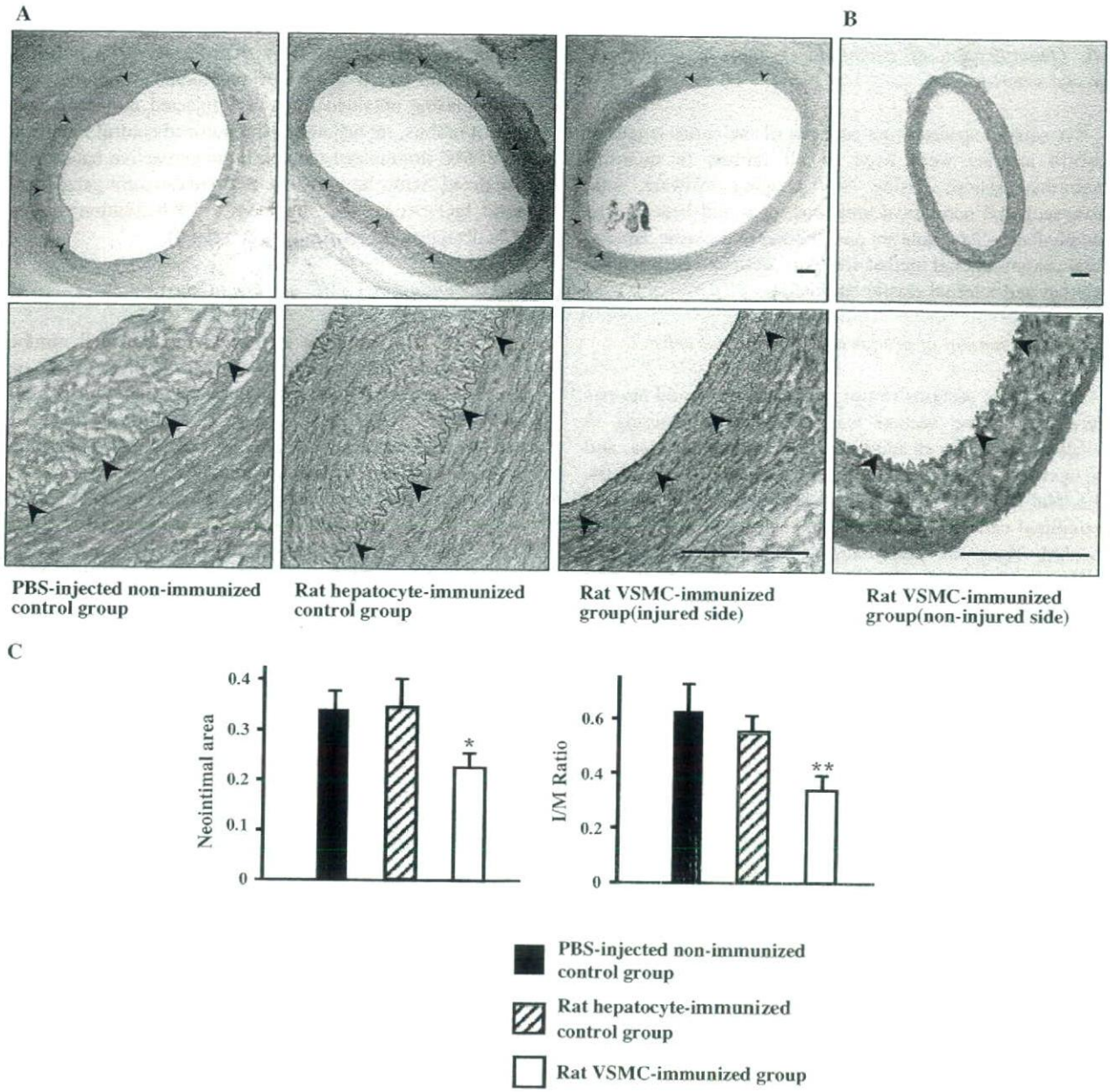

Fig. 1. (A) Representative light photomicrograph images showing injured carotid arteries from PBS-injected non-immunized control group, rat hepatocyte-immunized control group, and rat VSMC-immunized group at 4 weeks after balloon injury. Arrowhead indicates internal elastic lamina (IEL). Original magnifications are ×40 (upper) and ×200 (lower panels). Bars indicate 100 μm. (B) Representative light photomicrograph images showing the untouched contralateral common carotid artery from rat VSMC-immunized group. Arrowhead indicates internal elastic lamina (IEL). Original magnifications are ×40 (upper) and ×200 (lower panels). Bars indicate 100 μm. (C) Quantitative analysis of neointimal area and I/M ratio in rabbit carotid arteries at 4 weeks after injury in rat VSMC-immunized group (white bars), PBS-injected non-immunized control group (black bars), and rat hepatocyte-immunized control group (striped bars). Values are means ± SEM in each group. $*P<0.05$ vs. PBS-injected non-immunized control group and rat hepatocyte-immunized control group. $**P<0.05$ vs. PBS-injected non-immunized control group.

were presented as a percentage of the value for rat hepatocyte-immunized and control-immunized groups.

2.13. Identification of a target protein which rat VSMC-immunized immunoglobulin recognizes

Rabbit AT1a receptor cDNA was a generous gift from Dr. Raymond C. Harris (Vanderbilt Medical Center, Vanderbilt University). The complete coding site was excited and cloned into the expression vector pcDNA3 (Invitrogen), and pcDNA3 without any expression insert was used as the control vector. COS7 cells were purchased from the American Type Culture Collection (Manassas, VA) and cultured according to the manufacture's recommendations. COS7 cells were transfected by control pcDNA3 and rabbit AT1a receptor pcDNA3, respectively. The whole protein of these two groups of COS7 cells were resolved by SDS-PAGE, transferred to a PVDF membrane and probed with rabbit plasma obtained from PBS injected non-immunized control rabbits or rat hepatocyte-immunized control rabbits or rat VSMC-immunized rabbits respectively. Immunoreactive bands were visualized with horseradish peroxidase-conjugated anti-rabbit IgG (Amersham, England; 1:3000 dilution) and an ECL detection kit (Amersham, England).

2.14. Statistical analysis

Values represent means±SEM. Differences between groups were compared using a one-way analysis of variance test followed by Fisher protected least significant difference. $P<0.05$ was accepted as statistically significant.

3. Results

3.1. Blood analysis and general appearance of rabbits

Rat VSMC-immunization induced no significant changes in liver function, renal function and lipid profiles. Mean body weight and behavior of rabbits did not change by the immunization. In comparison with the PBS injected non-immunized control group, rat VSMC-immunization did not affect plasma IgG levels (284±61 mg/dl in PBS injected group vs. 268±44 mg/dl in rat VSMC-immunized group; P=NS).

3.2. Effect of rat VSMC immunization on the neointimal lesion formation

All animals developed concentric intimal lesions in response to the balloon injury. At 4 weeks after balloon injury, the mean neointimal area of PBS injected non-immunized group and rat hepatocyte-immunized control group were 0.339±0.036 and 0.350±0.041 mm^2, respectively (P=NS). The intimal lesion area was not significantly reduced by the rat hepatocytes control immunization. However, immunization with rat VSMCs significantly reduced the intimal lesion area (0.219±0.0286 mm^2; $P<0.05$ vs. PBS injected non-immunized group and rat

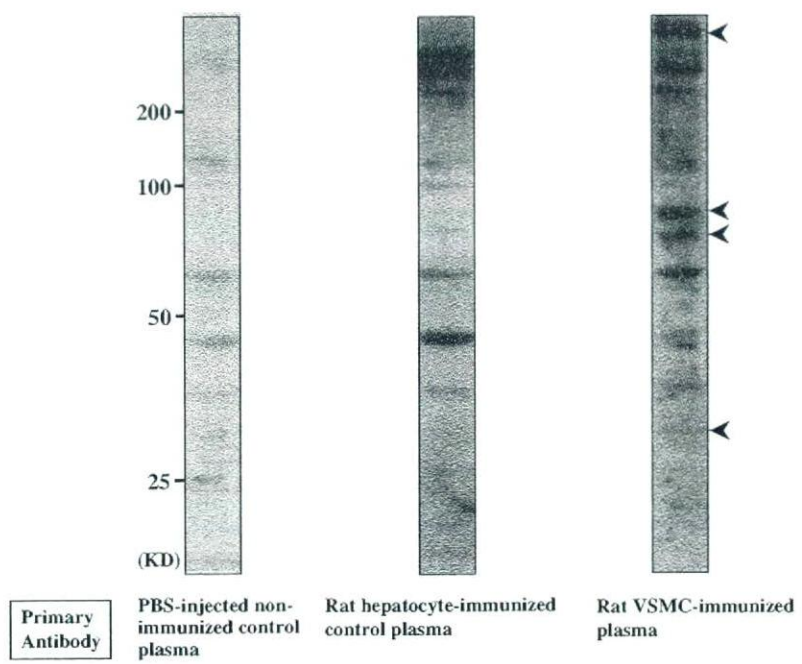

Fig. 2. Immunoblottings of proteins extracted from rabbit VSMCs using the plasma obtained from PBS injected non-immunized control rabbits (left), rat hepatocyte-immunized control rabbits (middle), or rat VSMC-immunized rabbits (right) as primary antibodies, respectively.

hepatocyte-immunized control group, Fig. 1A and C). The intimal/medial ratio was also significantly reduced in rat VSMC-immunized group (0.349±0.049) compared with PBS injected non-immunized group (0.662±0.114; $P<0.01$). There was no sign of infiltration of inflammatory cells at the contralateral common carotid artery (Fig. 1B). Immunization with rat VSMCs did not induce any pro-inflammatory effects on normal contractile VSMCs.

3.3. Rat VSMC immunization induced rabbit VSMC-reactive antibodies

To detect the antibodies, which were induced by xenogenic rat VSMC immunization, rabbit VSMCs proteins were resolved by SDS-PAGE, and immunoblotted with plasma obtained from the PBS injected non-immunized control rabbits, rat hepatocyte-immunized control rabbits ,

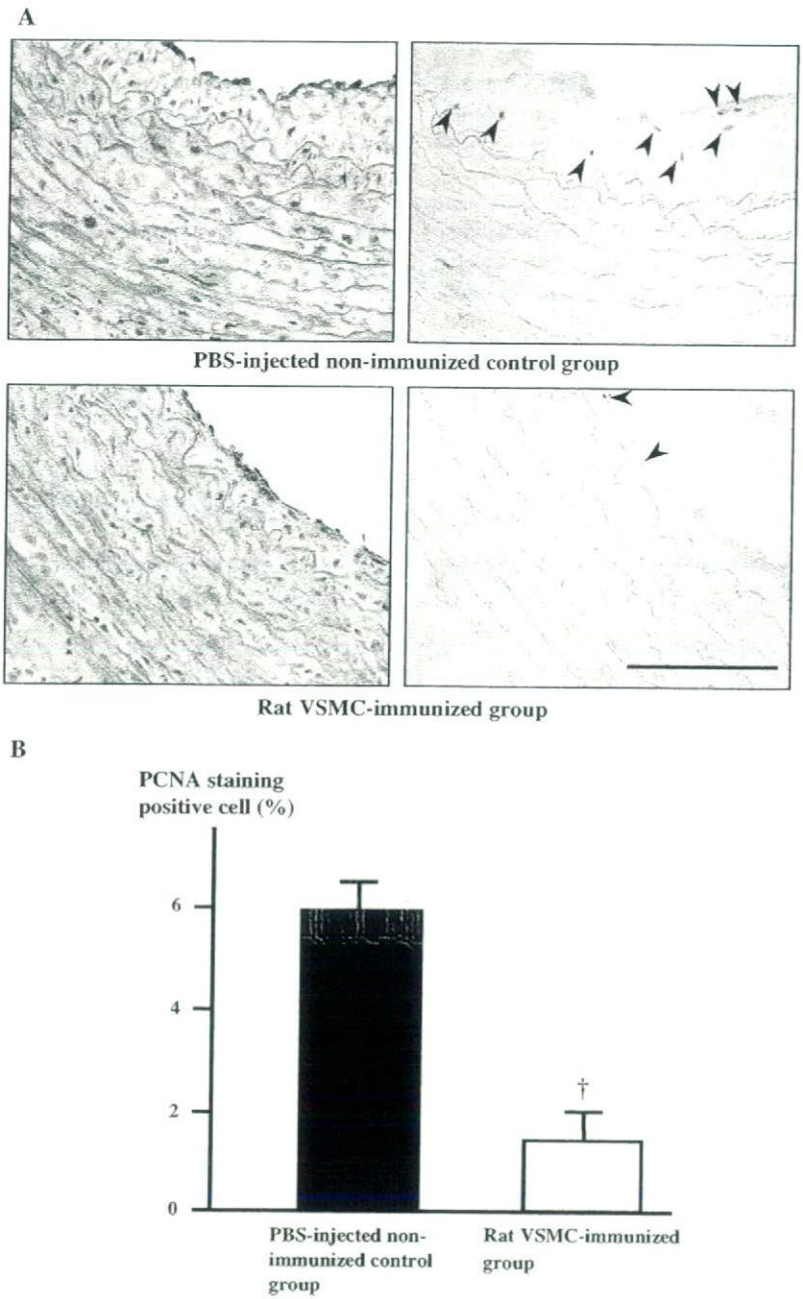

Fig. 3. (A) Photomicrographs of HE stainings (left panels) and PCNA immunostainings (right panels) in the neointima of injured carotid arteries at 2 weeks after balloon injury. Original magnification is ×200. A bar indicates 100 μm. (B) Quantitative analysis of PCNA positive proliferating cells in the neointima at 2 weeks after injury. Values are means±SEM of at least six rabbits in each group. †$P<0.01$ vs. PBS injected non-immunized control group.

or the VSMC-immunized rabbits. Only a few non-specific bands were detected when the plasma from the PBS injected non-immunized control rabbits was applied. Some bands were detected when the plasma from rat hepatocyte-immunized control rabbits was applied. In contrast, several new bands were clearly recognized in the immunoblot when we applied the plasma from rat VSMC-immunized rabbits (Fig. 2). It implies that the rat VSMC-immunized immunoglobulin recognized some new proteins of rabbit VSMCs that reacted with neither immunoglobulin from PBS injected non-immunized rabbits nor that from rat hepatocyte-immunized rabbits.

3.4. Effect of rat VSMC immunization on the proliferation and apoptosis of neointimal cells

To investigate whether the reduced neointimal lesion formation was due to the reduced proliferation of VSMCs in the neointimal lesion, the proliferation of neointimal VSMCs was investigated by the PCNA immunostaining on the day 14 after the injury (Fig. 3A). The percentage of PCNA-immunopositive cells was significantly reduced in VSMC-immunized group compared with in PBS injected control group (1.34%±0.49 vs. 5.78%±0.47, $P<0.01$, Fig. 3B).

Then to clarify the role of apoptosis in the reduction of neointimal formation, the TUNEL assay was carried out. As shown in Fig. 4, rat VSMC-immunization did not increase the number of TUNEL positive neointimal cells.

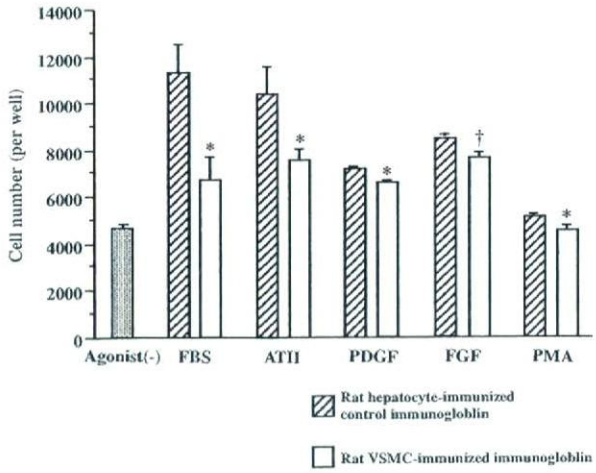

Fig. 5. Quantitative analysis of proliferation of cultured rabbit VSMCs treated with immunoglobulin obtained from rat hepatocyte-immunized control rabbits (striped bars) or rat VSMC-immunized rabbits (white bars). Values are means±SEM of separate six experiments in each group. †$P<0.01$ vs. the rat hepatocyte-immunized control group. *$P<0.05$ vs. PBS-injected non-immunized control group.

3.5. Effect of VSMC immunized immunoglobulins on rabbit VSMC proliferation and migration in vitro

The immunoglobulin (20 μg/ml) obtained from VSMC-immunized rabbits significantly suppressed rabbit VSMC cell numbers stimulated by FBS, ATII, PDGF, FGF, and PMA (Fig. 5) and rabbit VSMC migration stimulated by

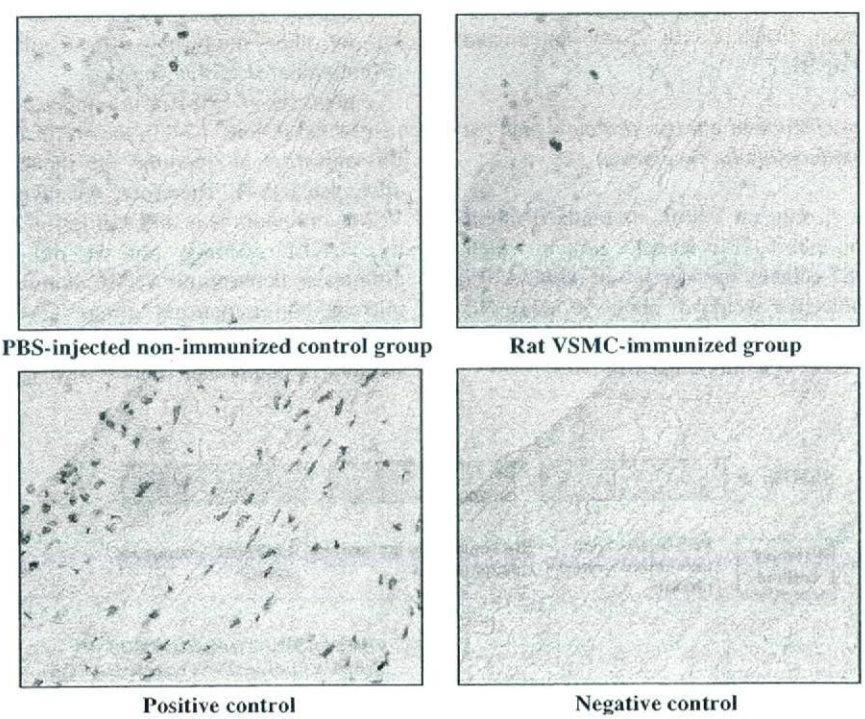

Fig. 4. Representative light photomicrograph images showing apoptosis in the neointimal cells using TUNEL technique.

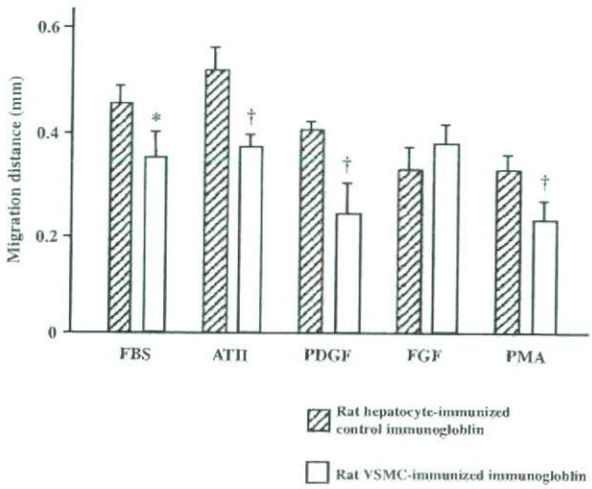

Fig. 6. Quantitative analysis of the migration distance evaluated by the maximally migrated point from the wounded edge in rat hepatocyte-immunized control group (striped bars) and in rat VSMC-immunized group (white bars), respectively. Values are means ± SEM of five separate experiments in each group. †$P<0.01$ vs. the rat hepatocyte-immunized control group. *$P<0.05$ vs. PBS-injected non-immunized control group.

FBS, ATII, PDGF, and PMA (Fig. 6), compared with that from rat hepatocyte-immunized control rabbits.

3.6. Effect of immunized immunoglobulin on VSMC viability

The rat VSMC-immunized immunoglobulin used in the proliferation and the migration assays did not alter rabbit VSMC viability assessed by WST-1 assay (rat hepartocyte-immunized control group: 100% vs. rat VSMC-immunized group: 106±8.6%, P=NS).

3.7. AT1a receptor may be one of a target protein which rat VSMC-immunized immunoglobulin recognizes

As shown in Fig. 7, only rat VSMC-immunized rabbit plasma recognized the rabbit AT1a receptor protein which was expressed in COS7 cells by transfection of rabbit AT1a receptor pcDNA3 (molecular weight is about 50 kDa). No bands were detected by immunoglobulin from PBS-injected rabbits or that from hepatocyte-immunized rabbits.

4. Discussion

In the present study, we demonstrated for the first time that, immunization with xenogenic rat synthetic VSMCs reduced neointimal formation after balloon injury, in association with induction of auto-antibodies against rabbit VSMCs. The VSMCs which contribute to form neointimal lesions are different in phenotype from ones in the normal media [31]. VSMCs in the normal media consisted of a contractile phenotype, whereas VSMCs which contribute to form neointimal lesions show a synthetic phenotype [32]. And the epitopes of VSMCs also may be different between the contractile phenotype and the synthetic phenotype. We used cultured rat VSMCs as the xenogenic immunogens against rabbits. These rat VSMCs are the synthetic phenotype, and therefore immunization with rat VSMCs was likely to induce various antibodies against the synthetic VSMCs. And importantly, it seemed that certain antibodies cross-reacted between rat and rabbit VSMCs.

As demonstrated in Fig. 2, when we applied rat VSMC-immunized plasma as the primary antibody, several new proteins of rabbit VSMCs were detected by the Western blot analysis, which were not detected when PBS injected non-immunized control plasma or rat hepatocyte-immunized control plasma was applied It implies that the rabbit plasma obtained from rat VSMC-immunized rabbits had an antibody response distinct from the one induced by PBS or rat hepatocytes. Importantly, as demonstrated in Fig. 1, only rat VSMC-immunization reduced the neointimal lesion formation after balloon injury. These results might implicate that the induced antibodies reacting with the synthetic VSMCs but not others might play critical roles in the reduction of neointimal area in this study.

Apoptosis of VSMCs is implicated in the formation of neointimal lesions [33]. In the aortic allograft model in rats, Plissonnier et al. reported the induction of apoptosis by alloantisera [34]. Therefore, we investigated apoptosis of VSMCs in both the neointimal lesion and the normal media by TUNEL staining, but we did not find significant differences between rat VSMC-immunized group and PBS injected non-immunized group. On the other hand, the proliferative capability of VSMCs estimated by PCNA staining in neointimal lesions was significantly suppressed

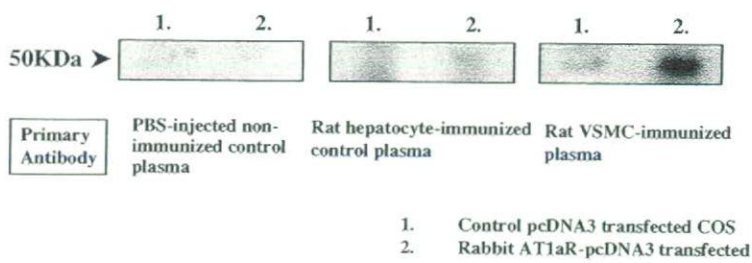

Fig. 7. The rabbit AT1a receptor protein expressed in COS7 cells by transfection of the rabbit AT1a receptor pcDNA3 was immunoblotted with PBS injected non-immunized control rabbit plasma (left panel), rat hapatocyte-immunized rabbit plasma (middle panel), or rat VSMC-immunized rabbit plasma (right panel), respectively. pcDNA3 without any expression inserts was used as the control transfection.

by rat VSMC-immunization (Fig. 3A and B), whereas no differences were detected in the media, at 2 weeks after balloon injury. Thus, proliferation of VSMCs in the neointima was suppressed by rat VSMC-immunization. This may be related to that neointimal lesions themselves may be more antigenic than the normal media. Plissonnier et al. reported that normal media was a "privileged" immunological site as compared to neointimal lesions in the vascular chronic rejection process in allotransplantation/immunization [35].

To further clarify the effects of the immunization on VSMC function, we performed in vitro assay. For in vitro assay, we purified immunoglobulin from plasma using a protein G column, because we needed to avoid the effects of many cytokines and growth factors which were contained in the immunized plasma. Therefore, in the study in vitro, we could investigate the direct effect of induced immunoglobulins. At first we compared viability of rabbit VSMCs between rat hepatocyte-immunized immunoglobulin treated control group and rat VSMC-immunized immunoglobulin treated group by use of WST-1 assay, and confirmed that viability of VSMC did not differ between two groups. Therefore VSMC-immunized immunoglobulin didn't have severe cell toxicity against VSMCs. The VSMC-immunized rabbits immunoglobulin significantly suppressed rabbit VSMC cell numbers stimulated by FBS, ATII, PDGF, FGF, and PMA (Fig. 5) and rabbit VSMC migration stimulated by FBS, ATII, PDGF, and PMA (Fig. 6). We applied immunoglobulins to the culture media, which bind only to the cell surface proteins. Therefore we speculate that rat VSMC-immunized immunoglobulin might bind to some surface proteins which globally regulate the proliferation and migration of rabbit VSMCs. As one of candidates for such surface proteins, we focused on AT1a receptor, since the inhibitory effects of VSMC-immunized rabbits immunoglobulin were prominent in ATII-induced proliferation and migration. As shown in Fig. 7, rat VSMC-immunized immunoglobulin was immunoreactive against the AT1a receptor protein which was expressed in COS7 cells by the rabbit AT1a receptor pcDNA3 transfection, whereas no bands were detected by immunoglobulin from PBS-injected rabbits or that from hepatocyte-immunized rabbits. Therefore, it is possible that rabbit AT1a receptor protein is one of target proteins which rat VSMC-immunized immunoglobulin recognizes and that binding of rat VSMC-immunized immunoglobulin to rabbit AT1a receptors might have inhibited the ATII signaling. Not only ATII signaling but almost all stimuli tested, however, were affected by the adjunction of rat VSMC-immunized immunoglobulin. Therefore it is likely that a much more global effect than the blocking effect on these receptors was involved. At the present time, we cannot show more detailed molecular mechanisms of the inhibitory effects of xenogenic VSMC immunization, and further investigation is needed.

This study demonstrated for the first time that xenogenic VSMC immunization significantly reduced neointimal formation in the balloon-injured carotid arteries. Our data indicate the possibility of immunotherapy for neointimal formation with xenogenic VSMCs by breaking immune tolerance against autologous VSMCs in a cross-reaction between the xenogenic homologs and self molecules, similar to the case of immunotherapy for tumor angiogenesis [36].

In the present study, rat VSMC-immunization didn't cause any serious side effects. The body weight and behavior of rabbits did not change by the immunization, and also blood analysis didn't show any significant changes in liver functions, renal functions, and lipid profiles. However, at the present time we cannot show the target protein(s) of VSMC-immunized immunoglobulin that regulates the functions of rabbit VSMC globally. Although further investigation on the target protein(s) and the possibility of immunological regulation is needed, immunological regulation shown in our study may be a new immunotherapy for vascular remodeling which forms neointimal lesion.

Acknowledgment

We appreciate Kiyoko Matsui for her secretarial assistance and technical support (cell culture, blood cell count, and animal care).

References

[1] Sriram V, Patterson C. Cell cycle in vasculoproliferative diseases: potential interventions and routes of delivery. Circulation 2001;103:2414–9.
[2] Breuss JM, Cejna M, Bergmeister H, Kadl A, Baumgartl G, Steurer S, et al. Activation of nuclear factor-kappa B significantly contributes to lumen loss in a rabbit iliac artery balloon angioplasty model. Circulation 2002;105:633–8.
[3] Stabile E, Zhou YF, Saji M, Castagna M, Shou M, Kinnaird TD, et al. Akt controls vascular smooth muscle cell proliferation in vitro and in vivo by delaying G1/S exit. Circ Res 2003;93:1059–65.
[4] Zhan Y, Kim S, Izumi Y, Izumiya Y, Nakao T, Miyazaki H, et al. Role of JNK, p38, and ERK in platelet-derived growth factor-induced vascular proliferation, migration, and gene expression. Arterioscler Thromb Vasc Biol 2003;23:795–801.
[5] Palinski W, Miller E, Witztum JL. Immunization of low density lipoprotein (LDL) receptor-deficient rabbits with homologous malondialdehyde-modified LDL reduces atherogenesis. Proc Natl Acad Sci U S A 1995;92:821–5.
[6] Zhou X, Paulsson G, Stemme S, Hansson GK. Hypercholesterolemia is associated with a T helper (Th) 1/Th2 switch of the autoimmune response in atherosclerotic apo E-knockout mice. J Clin Invest 1998;101:1717–25.
[7] Mallat Z, Besnard S, Duriez M, Deleuze V, Emmanuel F, Bureau MF, et al. Protective role of interleukin-10 in atherosclerosis. Circ Res 1999;85:e17–24.
[8] Afek A, George J, Gilburd B, Rauova L, Goldberg I, Kopolovic J, et al. Immunization of low-density lipoprotein receptor deficient (LDL-RD) mice with heat shock protein 65 (HSP-65) promotes early atherosclerosis. J Autoimmun 2000;14:115–21.

[9] Rittershaus CW, Miller DP, Thomas LJ, Picard MD, Honan CM, Emmett CD, et al. Vaccine-induced antibodies inhibit CETP activity in vivo and reduce aortic lesions in a rabbit model of atherosclerosis. Arterioscler Thromb Vasc Biol 2000;20:2106–12.
[10] Zhou X, Nicoletti A, Elhage R, Hansson GK. Transfer of CD4(+) T cells aggravates atherosclerosis in immunodeficient apolipoprotein E knockout mice. Circulation 2000;102:2919–22.
[11] Zhou X, Caligiuri G, Hamsten A, Lefvert AK, Hansson GK. LDL immunization induces T-cell-dependent antibody formation and protection against atherosclerosis. Arterioscler Thromb Vasc Biol 2001;21:108–14.
[12] Caligiuri G, Nicoletti A, Poirier B, Hansson GK. Protective immunity against atherosclerosis carried by B cells of hypercholesterolemic mice. J Clin Invest 2002;109:745–53.
[13] Maron R, Sukhova G, Faria AM, Hoffmann E, Mach F, Libby P, et al. Mucosal administration of heat shock protein-65 decreases atherosclerosis and inflammation in aortic arch of low-density lipoprotein receptor-deficient mice. Circulation 2002;106:1708–15.
[14] Binder CJ, Horkko S, Dewan A, Chang MK, Kieu EP, Goodyear CS, et al. Pneumococcal vaccination decreases atherosclerotic lesion formation: molecular mimicry between *Streptococcus pneumoniae* and oxidized LDL. Nat Med 2003;9:736–43.
[15] Caligiuri G, Rudling M, Ollivier V, Jacob MP, Michel JB, Hansson GK, et al. Interleukin-10 deficiency increases atherosclerosis, thrombosis, and low-density lipoproteins in apolipoprotein E knockout mice. Mol Med 2003;9:10–7.
[16] Fredrikson GN, Hedblad B, Berglund G, Alm R, Ares M, Cercek B, et al. Identification of immune responses against aldehyde-modified peptide sequences in apoB associated with cardiovascular disease. Arterioscler Thromb Vasc Biol 2003;23:872–8.
[17] Fredrikson GN, Soderberg I, Lindholm M, Dimayuga P, Chyu KY, Shah PK, et al. Inhibition of atherosclerosis in apoE-null mice by immunization with apoB-100 peptide sequences. Arterioscler Thromb Vasc Biol 2003;23:879–84.
[18] Mallat Z, Gojova A, Brun V, Esposito B, Fournier N, Cottrez F, et al. Induction of a regulatory T cell type 1 response reduces the development of atherosclerosis in apolipoprotein E-knockout mice. Circulation 2003;108:1232–7.
[19] Robertson AK, Rudling M, Zhou X, Gorelik L, Flavell RA, Hansson GK. Disruption of TGF-beta signaling in T cells accelerates atherosclerosis. J Clin Invest 2003;112:1342–50.
[20] Schiopu A, Bengtsson J, Soderberg I, Janciauskiene S, Lindgren S, Ares MP, et al. Recombinant human antibodies against aldehyde-modified apolipoprotein B-100 peptide sequences inhibit atherosclerosis. Circulation 2004;110:2047–52.
[21] Tupin E, Nicoletti A, Elhage R, Rudling M, Ljunggren HG, Hansson GK, et al. CD1d-dependent activation of NKT cells aggravates atherosclerosis. J Exp Med 2004;199:417–22.
[22] Nilsson J, Hansson GK, Shah PK. Immunomodulation of atherosclerosis: implications for vaccine development. Arterioscler Thromb Vasc Biol 2005;25:18–28.
[23] Nilsson J, Calara F, Regnstrom J, Hultgardh-Nilsson A, Ameli S, Cercek B, et al. Immunization with homologous oxidized low density lipoprotein reduces neointimal formation after balloon injury in hypercholesterolemic rabbits. J Am Coll Cardiol 1997;30:1886–91.
[24] Hayashi S, Watanabe N, Nakazawa K, Suzuki J, Tsushima K, Tamatani T, et al. Roles of P-selectin in inflammation, neointimal formation, and vascular remodeling in balloon-injured rat carotid arteries. Circulation 2000;102:1710–7.
[25] Hamaguchi A, Kim S, Izumi Y, Zhan Y, Yamanaka S, Iwao H. Contribution of extracellular signal-regulated kinase to angiotensin II-induced transforming growth factor-beta1 expression in vascular smooth muscle cells. Hypertension 1999;34:126–31.
[26] Faggin E, Puato M, Zardo L, Franch R, Millino C, Sarinella F, et al. Smooth muscle-specific SM22 protein is expressed in the adventitial cells of balloon-injured rabbit carotid artery. Arterioscler Thromb Vasc Biol 1999;19:1393–404.
[27] Kueng W, Silber E, Eppenberger U. Quantification of cells cultured on 96-well plates. Anal Biochem 1989;182:16–9.
[28] Sarkar R, Meinberg EG, Stanley JC, Gordon D, Webb RC. Nitric oxide reversibly inhibits the migration of cultured vascular smooth muscle cells. Circ Res 1996;78:225–30.
[29] Pukac L, Huangpu J, Karnovsky MJ. Platelet-derived growth factor-BB, insulin-like growth factor-I, and phorbol ester activate different signaling pathways for stimulation of vascular smooth muscle cell migration. Exp Cell Res 1998;242:548–60.
[30] Mosmann T. Rapid colorimetric assay for cellular growth and survival: application to proliferation and cytotoxicity assays. J Immunol Methods 1983;65:55–63.
[31] Nobuyoshi M, Kimura T, Ohishi H, Horiuchi H, Nosaka H, Hamasaki N, et al. Restenosis after percutaneous transluminal coronary angioplasty: pathologic observations in 20 patients. J Am Coll Cardiol 1991;17:433–9.
[32] Thyberg J, Blomgren K, Hedin U, Dryjski M. Phenotypic modulation of smooth muscle cells during the formation of neointimal thickenings in the rat carotid artery after balloon injury: an electron-microscopic and stereological study. Cell Tissue Res 1995;281:421–33.
[33] Mayr M, Xu Q. Smooth muscle cell apoptosis in arteriosclerosis. Exp Gerontol 2001;36:969–87.
[34] Plissonnier D, Henaff M, Poncet P, Paris E, Tron F, Thuillez C, et al. Involvement of antibody-dependent apoptosis in graft rejection. Transplantation 2000;69:2601–8.
[35] Plissonnier D, Nochy D, Poncet P, Mandet C, Hinglais N, Bariety J, et al. Sequential immunological targeting of chronic experimental arterial allograft. Transplantation 1995;60:414–24.
[36] Wei YQ, Wang QR, Zhao X, Yang L, Tian L, Lu Y, et al. Immunotherapy of tumors with xenogeneic endothelial cells as a vaccine. Nat Med 2000;6:1160–6.

An X-Ray Diffraction Study on Mouse Cardiac Cross-Bridge Function In Vivo: Effects of Adrenergic β-Stimulation

Ryuji Toh,* Masakazu Shinohara,* Tomofumi Takaya,* Tomoya Yamashita,* Shigeru Masuda,* Seinosuke Kawashima,* Mitsuhiro Yokoyama,* and Naoto Yagi†

*Division of Cardiovascular and Respiratory Medicine, Department of Internal Medicine, Kobe University Graduate School of Medicine, Kobe 650-0017, Japan; and †SPring-8/JASRI, Sayo, Hyogo 679-5198, Japan

ABSTRACT To investigate how β-stimulation affects the contractility of cardiac muscle, x-ray diffraction from cardiac muscle in the left ventricular free wall of a mouse heart was recorded in vivo. To our knowledge, this is the first x-ray diffraction study on a heart in a living body. After the R wave in electrocardiograms, the ratio of the intensities of the equatorial (1,0) and (1,1) reflections decreased for ~50 ms from a diastolic value of 2.1 to a minimum of 0.8, and then recovered. The spacing of the (1,0) lattice planes increased for ~90 ms from a diastolic value of 37.2 nm to a maximum of 39.1 nm, and then returned to the diastolic level, corresponding to ~10% stretch of sarcomere. Stimulation of β-adrenergic receptor by dobutamine (20 μg/kg/min) accelerated both the decrease in the intensity ratio, which reached a smaller systolic value, and the increase in the lattice spacing. However, the intensity ratio and spacing at the end-diastole were unchanged. The recovery of the lattice spacing during relaxation was also accelerated. The mass transfer to the thin filaments at systole in a β-stimulated heart was close to the peak value in twitch of frog skeletal muscle at 4°C, showing that the majority of cross-bridges have been recruited with few in reserve.

INTRODUCTION

Stimulation of cardiac β-adrenergic receptors has been known to enhance contractility of cardiac muscle through phosphorylation of various enzymes, including troponin-I, C-protein, and phospholamban (1–6). Although these effects have been extensively studied both physiologically and biochemically in isolated cardiac muscles and myocytes, they can be studied in a living body by only a limited number of methods. Lack of a molecular index that can be measured in vivo has made it difficult to study the mechanism of the β-stimulation. Since the overall influence of neurohumoral factors on functional properties of cardiac muscle can only be studied in vivo, it is important to develop a method to monitor contractility at the molecular level in a live animal. This is especially important when investigating the consequences of genetic alterations.

It is usually difficult to study murine, especially mouse, cardiac muscle in an isolated specimen under physiological conditions. Perfusion with oxygenated saline does not provide enough oxygen, and a heart tends to be in a hypoxic condition at physiological heart rates. Although an x-ray diffraction study on an intact rat papillary muscle has the advantage that force and sarcomere length can be measured simultaneously, such experiments have been made at a heart rate lower than 1 Hz (7,8). Since the heart rate is an important factor in cardiac physiology, which affects calcium handling and contractile force, it is necessary to make these experiments at higher heart rates. This is especially the case if the increase in the contractile force with increased heart rate (the staircase phenomenon) is due to a higher number of cross-bridges associated with the thin filament during diastole (9).

X-ray diffraction has been used to study contractility of cardiac muscle. It is a noninvasive method which enables us to study myosin cross-bridge activity in striated muscles (10). Two pieces of information can be obtained: one is the intensity ratio of the (1,0) and (1,1) equatorial reflections from the hexagonal lattice of myofilaments, which can be used as an index of the number of myosin cross-bridges formed during contraction (mass transfer from the thick to the thin filament). This correlates well with tension development in cardiac muscle, especially during the early phase of contraction under an isometric condition (9). Theoretically, the intensity ratio might be affected by a conformational change of cross-bridges. However, experiments on skeletal muscle showed that a force-generating conformational change does not affect the ratio (11). Thus, the change in the ratio is mostly caused by a mass movement from the thick filaments to the thin filaments due to cross-bridge formation. The other piece of available information is the (1,0) spacing of the lattice, which is equal to $\sqrt{3}/2$ of the distance between neighboring thick filaments. Since the volume of a cardiac cell remains approximately constant during a cardiac cycle (7), the lattice spacing can be used as an index of sarcomere length.

Recently, it was shown that diffraction patterns from a whole heart can be interpreted based on the orientation of muscle fibers in the heart (12), and a time-resolved x-ray diffraction study was made on a heart of a thoractomized rat (13). Here we applied this technique to a heart in a body of a

Submitted September 8, 2005, and accepted for publication November 18, 2005.

Ryuji Toh and Masakazu Shinohara contributed equally to this article.

Address reprint requests to N. Yagi, SPring-8/JASRI, Kouto, Sayo, Hyogo 679-5198, Japan. Tel.: 81-791-58-0908; Fax: 81-791-58-0830; E-mail: yagi@spring8.or.jp.

0006-3495/06/03/1723/06 $2.00

doi: 10.1529/biophysj.105.074062

living mouse to study physiological functions of myosin cross-bridges in vivo. Without thoractomizing, this is the first time the contractility in heart muscle was studied at a molecular level in a living body. Effects of β-stimulation by dobutamine were investigated.

METHODS

Animal preparation

Eight-week-old male mice (C57BL/6, purchased from CLEA Japan, Tokyo, Japan) were anesthetized with isoflurane (0.25–0.5%) and artificially ventilated (MiniVent, Hugo Sachs Elektronik, March-Hugstetten, Germany; stroke volume 200 μl, 250 strokes/min). To avoid strong x-ray diffraction spots from skeletal muscles (see below), part of the breast muscles was surgically removed. The mouse was fixed vertically in the x-ray beam, which entered the thorax from the third intercostal space. In this configuration, the x-ray beam passed through the upper part of the left ventricle, whose motion during a heart beat is smaller than in the lower part. The electrocardiogram was recorded with three electrodes (Fig. 1). Systemic blood pressure was measured by a computerized tail-cuff apparatus (MK-2000, Muromachi Kikai, Tokyo, Japan). The ventilator was stopped during an x-ray exposure (for ~2 s) to avoid movement due to respiration. Dobutamine was infused from carotid artery at a rate of 20 μg/kg/min. The animal experiments were conducted in accordance with the guidelines of SPring-8 for care and welfare of experimental animals.

X-ray diffraction methods

X-ray diffraction experiments were conducted at BL40XU in the SPring-8 third generation synchrotron radiation facility (Harima, Hyogo, Japan) (14). The peak x-ray energy was adjusted to 15.0 keV. This high energy ensured sufficient penetration of x-rays through the body of a mouse. The x-ray flux was adjusted by the front-end slits and aluminum absorbers to $\sim 3 \times 10^{12}$ photons/s. The beam size was ~0.10 mm vertically, 0.25 mm horizontally at the specimen.

The x-ray detector was an x-ray image intensifier with a beryllium window (V5445P, Hamamatsu Photonics, Hamamatsu, Japan) (15) coupled by a tandem lens to a fast charge-coupled device (CCD) camera (C4880-80-24A, Hamamatsu Photonics). The time resolution was 15 ms/frame. An x-ray shutter was opened for 1.1 s, and 70 successive frames were recorded.

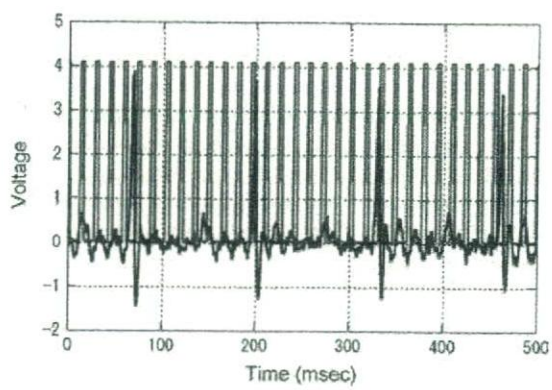

FIGURE 1 Electrocardiogram (*blue*) and frame timing of the CCD camera (*red*) during time-resolved x-ray recording. There is noise in the electrocardiogram from the power line (60 Hz) but sharp QRS peaks and preceding small Q peaks are clearly seen. The rising edge of the frame timing pulses corresponds to the beginning of a new frame.

The specimen-to-detector distance was 3.2 m. The lattice spacing was calibrated with the third-order meridional reflection from the thick filament of frog skeletal muscle at 1/14.34 nm^{-1}. Both the electrocardiogram and the frame timing signal from the CCD camera were recorded with a data acquisition system with 1-ms sampling.

Experimental protocol

Since there are layers of skeletal muscles in the path of the x-ray beam, diffraction patterns from a mouse heart in vivo are always mixed with equatorial diffraction spots from skeletal muscles. With a mouse positioned vertically and an x-ray beam passing between the third and fourth ribs, usually two sets of spots were found in the directions of 10 o'clock and 4 o'clock, and 9 o'clock and 3 o'clock (Fig. 2). The areas between these spots were free from reflections due to skeletal muscles. Initially, the x-ray beam was positioned in the left side of a mouse thorax (Fig. 3, position *A*). Then, the mouse was moved across the beam horizontally so that its left ventricular free wall came into the beam (Fig. 3, position *B*). When the x-ray beam passed through the epicardium of the free wall, the equatorial reflections, which appear as spots (12), were observed in the directions similar to those of skeletal muscles. Thus, the epicardium surface plane seems to be approximately vertical in the mouse body. At this position, the movement of the heart due to beating shifted the heart in and out of the beam in every heart beat, making it impossible to observe the diffraction pattern continuously. When the mouse was moved further and the x-ray beam passed through the deeper layer of the free wall (Fig. 3, position *C*), the equatorial diffraction pattern became arcs (12). At this stage, it was still difficult to observe the diffraction pattern continuously because the beam passed through different regions of the wall in diastole and systole. When the mouse was moved further in the beam (Fig. 3, position *D*), the diffraction pattern appeared as a ring or a long arc with maximum intensity in the direction perpendicular to the diffraction from skeletal muscles (Fig. 2). The diffraction pattern was continuously observed during a heart beat, allowing us to study the molecular changes throughout a cardiac cycle. Thus, experiments were made under this condition. The x-ray beam is presumed to be passing through endocardium and left ventricle (12). Marking the recorded region after an experiment, with an x-ray flux three orders of magnitude higher than that used for the x-ray diffraction measurement, confirmed that the beam actually passed through the left ventricular free wall.

The x-ray recording was repeated up to 10 times (average 5.3 recordings) with a horizontal shift of a mouse by 0.2 mm. The data were analyzed only when distinct diffraction from cardiac muscle was observed throughout a cardiac cycle. After dobutamine infusion, the mouse was moved vertically by ~0.2 mm to avoid radiation damage, and the recordings were repeated. No sign of radiation damage, such as broadening or weakening of the equatorial intensity profile, was seen.

Since the x-ray recording was not in synchrony with the cardiac cycle, it was necessary to determine correspondence between the x-ray frames and the cardiac cycle. At the heart rate of 400–500 per min, there were 8–9 frames per each cycle, and 7–8 cycles were recorded in each x-ray recording, which lasted for $15 \times 70 = 1050$ ms. In this study, only the data with nine frames per cycle were analyzed. The frames that contained the R wave in the electrocardiogram (Fig. 1) were used as the first frame of a cycle (end-diastole). Then, frames in the same phase of the cycle were averaged. Thus, for each recording, a set of images was obtained. As the R wave could take place any time within a frame, the data had an ambiguity of one frame (15 ms) in time. This ambiguity is averaged out because, in total, data from 53 and 58 recordings were used for the baseline and dobutamine conditions, respectively.

Data analysis

Diffraction in the region of the x-ray pattern without contribution from skeletal muscles was circularly averaged. The background was fitted with a cubic spline function, and the area above the background was used as the

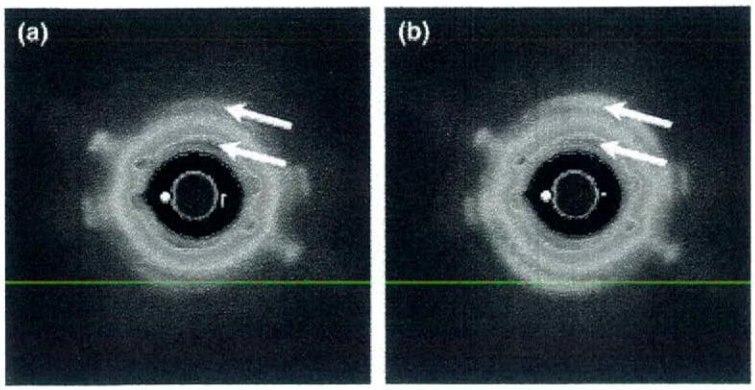

FIGURE 2 X-ray diffraction patterns from a heart in vivo. (*a*) In end-diastole (first frame), (*b*) in systole (fourth frame). The intensity distribution is shown in pseudocolor. The four spots are from skeletal muscles. The rings in the rest of the pattern (*arrows*) are from cardiac muscle: the inner one is the (1,0), and the outer (1,1) equatorial reflection. These are averages of six diffraction patterns from a normal mouse.

diffraction peak (Fig. 4). The integrated area was used as the integrated intensity, and the center of gravity of the (1,0) reflection was converted to the (1,0) lattice spacing. The integrated intensity of the (1,1) reflection obtained this way is underestimated by $\sqrt{3}$ compared to that of the (1,0) reflection because the intensity is averaged, not summed, along an arc. Thus, the (1,1) intensity was multiplied by $\sqrt{3}$. Since the intensity of each equatorial reflection depends on the thickness of the sample, which changes considerably across a heart, the ratio of the intensities of the (1,0) and (1,1) reflections (I(1,0)/I(1,1)) was used as an index of the equatorial intensity change.

Then, data from different x-ray recordings were analyzed. Results from recordings on each mouse were averaged, providing a set of intensity ratios and lattice spacings for each mouse over frames. Then, data sets from 10 mice were treated statistically. The same procedure was used on the data taken after dobutamine infusion.

The half-time of contraction and relaxation was obtained by the following method: 1), The intensity ratio or lattice spacing in the first frame was taken as a diastolic level. 2), The smallest intensity ratio or the largest lattice spacing value was taken as a systolic level. 3), The average of the diastolic and systolic levels was taken as the midlevel. 4), The time when the intensity ratio or lattice spacing crossed the midlevel during the early or late phase of a heart beat was obtained by interpolation between frames and taken as the half-time of contraction or relaxation.

Using the ratio of the (1,0) and (1,1) intensities (I(1,0)/I(1,1)), the electron-density distribution in the transverse section of the hexagonal myofilament lattice was calculated by Fourier synthesis. From this, the mass associated with the thin filaments was estimated following the method of Haselgrove and Huxley (10) on the assumption that the lowest density in the electron-density map represented the background level. The "apparent" thin-filament mass thus calculated was interpreted as consisting of the thin filament and the myosin heads present in the vicinity of the thin filament. The mass of the thin filament was approximated by assuming that no myosin heads are present in the vicinity of the thin filament at the resting state. Then, by subtracting this from the apparent thin-filament mass, the mass of heads associated with the thin filament was obtained. The same procedure was done with the intensity ratio obtained in the rigor state, and the total mass of heads can be obtained by assuming that all heads are attached to the thin filament. From these masses of heads, the proportion of heads present in the vicinity of thin filaments was calculated.

All data are expressed as mean ± SD. Differences were analyzed using Student's paired *t*-test with $p < 0.05$ being regarded as statistically significant.

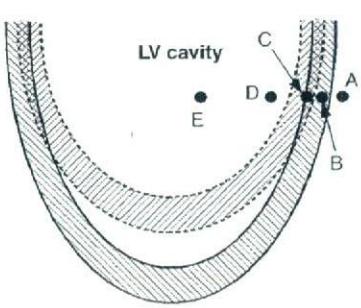

FIGURE 3 Positions of the x-ray beam relative to the left ventricle. The shaded areas represent a left ventricular free wall. The area between solid curves is a wall in diastole, and that between broken curves a wall in systole. At position *A*, the beam is out of the heart. At *B*, the beam is passing through the epicardium in diastole but out of the heart in systole. At *C*, the beam is always in the wall but it is in the epicardium in diastole and in the endocardium in systole. At *D*, the beam is always passing through the wall on both sides of the heart. At *E*, the beam also passes through the wall on both sides but absorption by blood in the cavity hampers the x-ray measurement. In the actual experiment, a mouse (hence a heart) was moved relative to a fixed x-ray beam.

RESULTS

Fig. 2 shows x-ray diffraction patterns from a mouse heart in vivo at end-diastole and systole. Although diffraction spots from skeletal muscles are superposed, arcs of equatorial diffraction from cardiac muscles are clearly seen. The origin of the reflection can be assigned without ambiguity because the skeletal muscle has a smaller filament lattice spacing and hence the reflections appeared at a larger radius. When the region where the equatorial reflections from cardiac muscle were strong, it was possible to subtract background from other tissues such as skin, lung, and skeletal muscle (Fig. 4). Fig. 5 *a* (*open squares*) shows the time course of changes in the (1,0)/(1,1) intensity ratio during a cardiac cycle at baseline. The diastolic intensity ratio was ~2.1 at end-diastole and decreased to a minimum of 0.8 in ~50 ms, which is comparable to the ratios observed in rat heart muscle (13).

Fig. 5 *b* (*open squares*) shows the time course of changes in the (1,0) lattice spacing at baseline. The lattice spacing at end-diastole was 37.2 nm and increased to 39.1 nm within

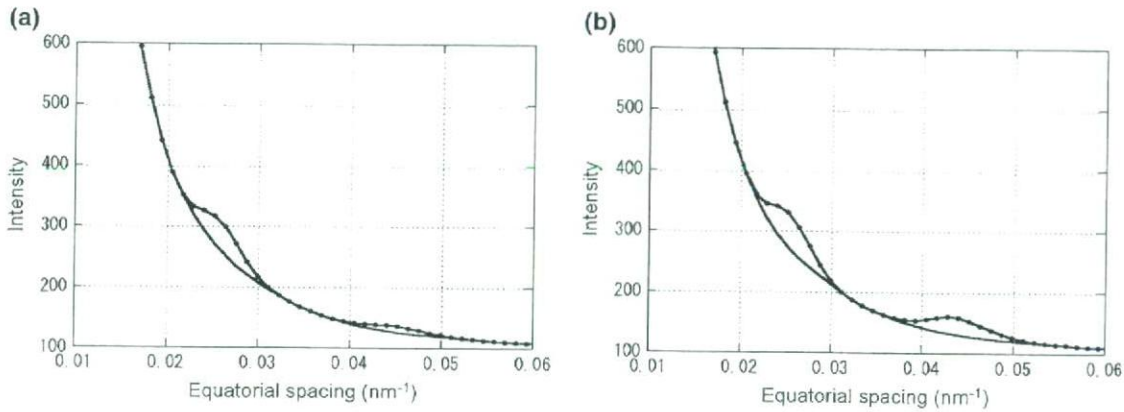

FIGURE 4 Intensity profiles of the (1,0) and (1,1) equatorial peaks. (a) in end-diastole, (*b*) in systole. The data were from Fig. 3, integrated within arcs of 10.5 o'clock through 2 o'clock and its opposite side. The background was drawn using a spline function.

~90 ms after the R wave in the electrocardiogram. If strict constant-volume behavior is assumed, this corresponds to ~10% shortening of sarcomere. The lattice spacing continued to increase after the intensity ratio started to increase (that is, after the muscle began to relax), until the mitral valve opened and the left ventricular volume began to increase.

The experiment was repeated after dobutamine had been infused for 10 min (20 μg/kg/min). The heart rate did not change significantly (from 446 $\pm$ 26 to 449 $\pm$ 26 beats per min, $n = 10$). The systemic blood pressure increased significantly from 83.9 $\pm$ 13.1 to 97.1 $\pm$ 14.9 mmHg ($n = 10$). Fig. 5 *a* (*solid circles*) shows the change in the (1,0)/(1,1) intensity ratio under the influence of dobutamine. The second, third, and fourth data points between 20 and 60 ms after the R wave were significantly lower than those in the control mouse, showing a faster and larger shift of mass of cross-bridges. Fig. 5 *b* (*solid circles*) shows the time course of the (1,0) spacing change. The third and fourth data points are significantly larger than those in the control mouse, showing a faster shortening of muscle. The half-time of the reduction in the intensity ratio was significantly shortened by dobutamine (24.4 $\pm$ 1.4 to 20.3 $\pm$ 1.3 ms, $n = 10$), and that of the lattice spacing was also shortened (52.8 $\pm$ 5.9 to 38.3 $\pm$ 1.8 ms, $n = 10$). The half-relaxation time of the lattice spacing was significantly shorter after dobutamine (112.6 $\pm$ 3.0 to 106.8 $\pm$ 2.8 ms, $n = 10$). Since the larger change in the lattice spacing suggests larger sarcomere shortening, the systolic intensity ratio might be affected by a larger filament overlap in the presence of dobutamine. However, since cardiac muscle normally works at a sarcomere length shorter than 2 μm where the thick and thin filaments are fully overlapped, this effect is not considered significant.

After an experiment, a mouse was killed by overdose of pentobarbital and left for 30 min. Then, a diffraction pattern in the rigor state was recorded. The (1,0)/(1,1) intensity ratio was 0.30 $\pm$ 0.08 ($n = 8$).

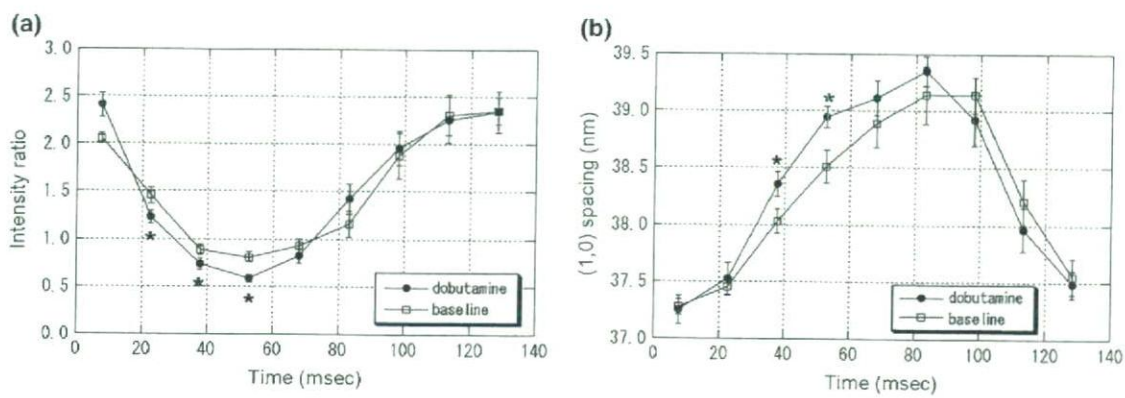

FIGURE 5 Effects of β-stimulation on the cross-bridge activity of mouse heart muscle. (*a*) The (1,0)/(1,1) intensity ratio, (*b*) the (1,0) lattice spacing. The abscissa is the time after the R wave in the electrocardiogram. Open squares represent data obtained before dobutamine infusion, and solid circles after dobutamine infusion (20 μg/kg/ml). The error bars represent the standard error of the mean of data from 10 mice. The asterisks indicate the data points that are statistically different in paired *t*-tests between baseline and dobutamine data.